

NuFit-6.0: Updated global analysis of three-flavor neutrino oscillations

Ivan Esteban,^{a,b} M. C. Gonzalez-Garcia,^{c,d,e} Michele Maltoni,^f Ivan Martinez-Soler,^g
João Paulo Pinheiro,^c Thomas Schwetz^h

^a*Department of Physics, University of the Basque Country UPV/EHU, PO Box 644, 48080 Bilbao, Spain*

^b*EHU Quantum Center, University of the Basque Country UPV/EHU*

^c*Departament de Física Quàntica i Astrofísica and Institut de Ciències del Cosmos, Universitat de Barcelona, Diagonal 647, E-08028 Barcelona, Spain*

^d*Institució Catalana de Recerca i Estudis Avançats (ICREA), Pg. Lluís Companys 23, 08010 Barcelona, Spain.*

^e*C.N. Yang Institute for Theoretical Physics, State University of New York at Stony Brook, Stony Brook, NY 11794-3840, USA*

^f*Instituto de Física Teórica UAM/CSIC, Calle de Nicolás Cabrera 13-15, Universidad Autónoma de Madrid, Cantoblanco, E-28049 Madrid, Spain*

^g*Institute for Particle Physics Phenomenology, Durham University, South Road, DH1 3LE, Durham, UK*

^h*Institut für Astroteilchenphysik, Karlsruher Institut für Technologie (KIT), 76021 Karlsruhe, Germany*

E-mail: ivan.esteban@ehu.eus, concha.gonzalez-garcia@stonybrook.edu,
michele.maltoni@csic.es, ivan.j.martinez-soler@durham.ac.uk,
joaopaulo.pinheiro@fqa.ub.edu, schwetz@kit.edu

ABSTRACT: We present an updated global analysis of neutrino oscillation data as of September 2024. The parameters θ_{12} , θ_{13} , Δm_{21}^2 , and $|\Delta m_{3\ell}^2|$ ($\ell = 1, 2$) are well-determined with relative precision at 3σ of about 13%, 8%, 15%, and 6%, respectively. The third mixing angle θ_{23} still suffers from the octant ambiguity, with no clear indication of whether it is larger or smaller than 45° . The determination of the leptonic CP phase δ_{CP} depends on the neutrino mass ordering: for normal ordering the global fit is consistent with CP conservation within 1σ , whereas for inverted ordering CP-violating values of δ_{CP} around 270° are favored against CP conservation at more than 3.6σ . While the present data has in principle $2.5\text{--}3\sigma$ sensitivity to the neutrino mass ordering, there are different tendencies in the global data that reduce the discrimination power: T2K and NOvA appearance data individually favor normal ordering, but they are more consistent with each other for inverted ordering. Conversely, the joint determination of $|\Delta m_{3\ell}^2|$ from global disappearance data prefers normal ordering. Altogether, the global fit including long-baseline, reactor and IceCube atmospheric data results into an almost equally good fit for both orderings. Only when the χ^2 table for atmospheric neutrino data from Super-Kamiokande is added to our χ^2 , the global fit prefers normal ordering with $\Delta\chi^2 = 6.1$. We provide also updated ranges and correlations for the effective parameters sensitive to the absolute neutrino mass from β -decay, neutrinoless double-beta decay, and cosmology.

KEYWORDS: neutrino oscillations, solar and atmospheric neutrinos

Contents

1	Introduction	1
2	Global analysis	2
3	Status of neutrino mass ordering, leptonic CP violation, and θ_{23}	7
3.1	Updates from T2K and NOvA	7
3.2	Effects from $\nu_\mu/\bar{\nu}_\mu$ versus $\bar{\nu}_e$ disappearance	12
3.3	Sensitivity to the neutrino mass ordering	15
4	Updates in the “12” sector	18
5	Projections on neutrino mass scale observables	19
6	Summary	22
A	List of data used in the analysis	23
B	IceCube 2019	25
C	Assumed true values for the MO test	26

1 Introduction

The global analysis of neutrino oscillation data provides us with the unique comprehensive description of the non-trivial flavor structure of leptons. Although in the last years some efforts are being put forward by the experimental collaborations for combined analysis of their results [1–3], the main task still falls on the work of phenomenological groups [4–6]. Over the last decade these global analyses have provided consistent results with very good quantitative agreement on the dominant effects. In a nutshell, it is found that mass-driven oscillations between three neutrino states of different mass and three different mixing angles account for the vast majority of the results. And, when redundant, the results from different experiments on the dominant effects in this picture are statistically compatible.

In addition, three-neutrino oscillation effects which are subdominant or quantitatively small in present experiments include the mass ordering (MO) of the three states, the possible maximality of one of the mixing angles (θ_{23} in the standard parametrization), and the amount of leptonic CP violation. They remain open questions in the present experimental landscape and constitute the main goal of the upcoming generation of experiments [7–9]. The phenomenological analysis finds minor differences in these subdominant effects, and their statistical significance has been varying with time as the running experiments

accumulate more statistics and update their analyses. This, in fact, is one of the main motivations for the redundancy of the global phenomenological analysis, providing unbiased tests for the consistency over time of the emerging picture.

In this effort, this work contains the latest analysis within the NuFIT program, NuFIT 6.0, which incorporates a number of changes and updates since our last published analysis in 2020 [4]. In the solar neutrino sector, the new generation of Standard Solar Models [10] are now used for the predictions, and the full day-night spectrum from the phase-IV of Super-Kamiokande [11] together with the final spectra from Borexino phases-II [12] and III [13] are included. For the long baseline (LBL) reactor data, we have updated the reactor antineutrino fluxes used for the predictions to the latest Daya-Bay measurements [14], and results from SNO+ [15–17] are included in the global analysis for the first time. From reactors at medium baseline (MBL), we include the most up-to-date Daya-Bay spectral data [18]. Updates in the LBL accelerator analysis include incorporating the latest samples and simulation updates of T2K [2], and the doubled statistics of NOvA neutrino samples [3]. A new independent analysis of atmospheric neutrinos from 3 years of IceCube/DeepCore data [19, 20] has been incorporated. Finally, the effect of the updated χ^2 maps provided by the collaborations for the analysis of the latest atmospheric neutrino samples in Super-Kamiokande [21, 22] and IceCube/DeepCore [23, 24] is accounted for.

The outline of the paper is as follows. In Sec. 2 we present the results of our global analysis, providing best-fit values and 1-dimensional and 2-dimensional confidence regions for the 6 oscillation parameters, and we discuss the global determination of leptonic CP violation. In Sec. 3 we discuss in some detail the various tendencies in the global data, focusing on experiments sensitive to the large mass splitting $\Delta m_{3\ell}^2$ ($\ell = 1, 2$). In Sec. 3.1 we discuss the compatibility among T2K and NOvA appearance data, whereas in Sec. 3.2 we consider the global combination of disappearance data (which includes accelerator, reactor and atmospheric neutrinos), presenting a detailed study of the compatibility among different combinations of datasets. In Sec. 3.3 we discuss in detail the sensitivity to the neutrino mass ordering in terms of a proper hypothesis test. Section 4 focuses on the “solar sector” governed by Δm_{21}^2 , especially in light of the latest developments in solar models. In Sec. 5 we provide the relevant correlations between absolute neutrino mass observables. We summarize our results in Section 6, and provide a list of all the used data in Appendix A. In Appendix B we describe our analysis of IceCube data, and in Appendix C we provide more details on the mass ordering test.

2 Global analysis

We start by presenting the results of the NuFIT 6.0 global fit. Parametrization conventions and technical details on our global analysis can be found in Ref. [25]. In particular, we use the standard parametrization of the 3×3 unitary leptonic mixing matrix [26, 27]

$$U = \begin{pmatrix} 1 & 0 & 0 \\ 0 & c_{23} & s_{23} \\ 0 & -s_{23} & c_{23} \end{pmatrix} \cdot \begin{pmatrix} c_{13} & 0 & s_{13}e^{-i\delta_{\text{CP}}} \\ 0 & 1 & 0 \\ -s_{13}e^{i\delta_{\text{CP}}} & 0 & c_{13} \end{pmatrix} \cdot \begin{pmatrix} c_{12} & s_{12} & 0 \\ -s_{12} & c_{12} & 0 \\ 0 & 0 & 1 \end{pmatrix} \cdot \mathcal{P}, \quad (2.1)$$

where $c_{ij} \equiv \cos \theta_{ij}$ and $s_{ij} \equiv \sin \theta_{ij}$, with angles $\theta_{ij} \in [0, \pi/2]$ and phase $\delta_{\text{CP}} \in [0, 2\pi]$, such that $\delta_{\text{CP}} \neq 0, \pi$ implies CP violation in neutrino oscillations in vacuum [28–30]. Here $\mathcal{P} = I$ for Dirac neutrinos and $\mathcal{P} = \text{diag}(e^{i\alpha_1}, e^{i\alpha_2}, 1)$ for Majorana neutrinos, a matrix that plays no role in neutrino oscillations [29, 31]. In this convention, there are two non-equivalent orderings for the neutrino masses, namely normal ordering (NO) with $m_1 < m_2 < m_3$, and inverted ordering (IO) with $m_3 < m_1 < m_2$. In particular, in what follows we use the definition

$$\Delta m_{3\ell}^2 \quad \text{with} \quad \begin{cases} \ell = 1 & \text{for } \Delta m_{3\ell}^2 > 0: \text{ normal ordering (NO)}, \\ \ell = 2 & \text{for } \Delta m_{3\ell}^2 < 0: \text{ inverted ordering (IO)}. \end{cases} \quad (2.2)$$

The analysis includes all data available up to September 2024 which, for convenience, we list in Appendix A with the corresponding references. As is customary in the NuFIT analysis since v4.0 [25], we show two versions of the analysis. These versions differ in the inclusion of atmospheric neutrino results, for which there is not enough information for us to make an independent analysis comparable to that performed by the collaborations. In NuFIT 6.0, this is the case for the atmospheric neutrino data from Super-Kamiokande phases 1-5 (SK-atm) and from the latest 9.3-year result from IceCube/DeepCore (IC24). For those, we use their tabulated χ^2 maps provided in Refs. [22] and [24], respectively, which we can combine with our global analysis for the solar, reactor and LBL experiments. We note that for IceCube/DeepCore we have performed an independent analysis of their previous 3-year atmospheric neutrino data sample [19, 20], which we do include in the version of the analysis without tabulated χ^2 maps. In what follows, we refer as «IC19 w/o SK-atm» to the analysis variant without tabulated χ^2 maps, and as «IC24 with SK-atm» to the analysis variant that includes the tabulated SK-atm and IC24 χ^2 maps instead of our 3-year IceCube/DeepCore analysis.

A selection of the results of our global fit are displayed in Fig. 1 (one-dimensional $\Delta\chi^2$ curves) and Fig. 2 (two-dimensional projections of confidence regions). In Table 1 we give the best-fit values as well as 1σ and 3σ confidence intervals for the oscillation parameters in both mass orderings, relative to the local best-fit points in each ordering. Additional figures and tables corresponding to this global analysis can be found in the NuFIT webpage [32].

With these results, we obtain the following 3σ relative precision of each parameter x , defined as $2(x^{\text{up}} - x^{\text{low}})/(x^{\text{up}} + x^{\text{low}})$, where x^{up} (x^{low}) is the upper (lower) bound on x at the 3σ level:

$$\begin{aligned} \theta_{12} : 13\%, \quad \theta_{13} : \begin{cases} \text{NO } 8.1\% [8.2\%], \\ \text{IO } 7.8\% [7.9\%], \end{cases} \quad \theta_{23} : \begin{cases} \text{NO } 21\% [19\%], \\ \text{IO } 20\% [18\%], \end{cases} \\ \Delta m_{21}^2 : 15\%, \quad |\Delta m_{3\ell}^2| : \begin{cases} \text{NO } 5.6\% [5.1\%], \\ \text{IO } 5.8\% [5.1\%], \end{cases} \quad \delta_{\text{CP}} : \begin{cases} \text{NO } 100\% [98\%], \\ \text{IO } 54\% [55\%], \end{cases} \end{aligned} \quad (2.3)$$

where the numbers between brackets show the impact of including IC24 and SK-atm. We note that given the non-Gaussianity of $\Delta\chi^2(\delta_{\text{CP}})$, the above estimated precision for δ_{CP} can only be taken as indicative, in particular for NO.

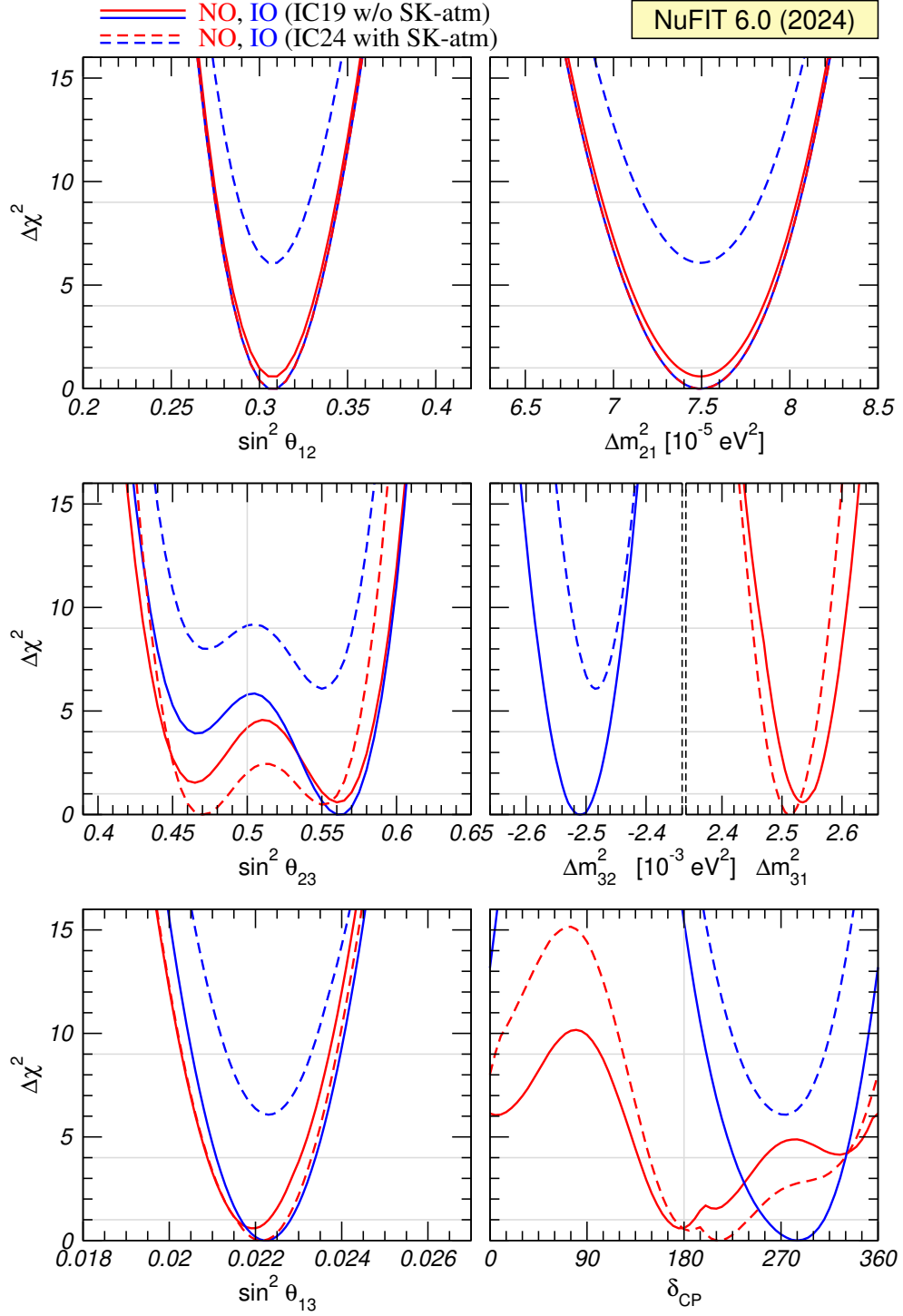


Figure 1. Global 3ν oscillation analysis. We show $\Delta\chi^2$ profiles minimized with respect to all undisplayed parameters. The red (blue) curves correspond to Normal (Inverted) Ordering. Solid and dashed curves correspond to the two variants of the analysis as described in the labels.

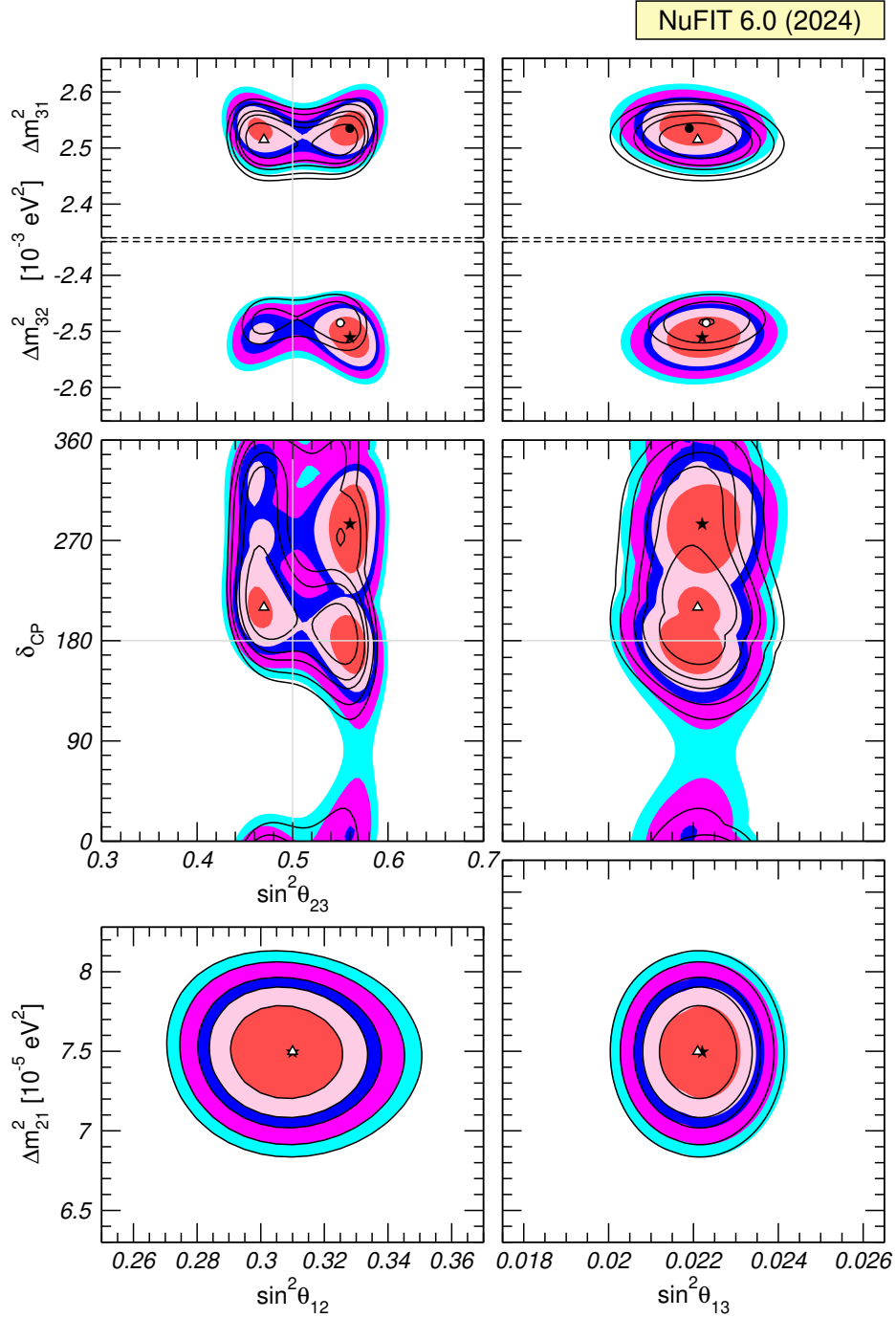


Figure 2. Global 3ν oscillation analysis. Each panel shows the two-dimensional projection of the allowed six-dimensional region after minimization with respect to the undisplayed parameters. The regions in the four lower panels are obtained from $\Delta\chi^2$ minimized with respect to the mass ordering. The different contours correspond to 1 σ , 90%, 2 σ , 99%, 3 σ CL (2 dof). Colored regions (black contours) correspond to the variant with IC19 and without SK-atm (with IC24 and with SK-atm).

		Normal Ordering ($\Delta\chi^2 = 0.6$)		Inverted Ordering (best fit)	
		bfp $\pm 1\sigma$	3σ range	bfp $\pm 1\sigma$	3σ range
IC19 without SK atmospheric data	$\sin^2 \theta_{12}$	$0.307^{+0.012}_{-0.011}$	0.275 \rightarrow 0.345	$0.308^{+0.012}_{-0.011}$	0.275 \rightarrow 0.345
	$\theta_{12}/^\circ$	$33.68^{+0.73}_{-0.70}$	31.63 \rightarrow 35.95	$33.68^{+0.73}_{-0.70}$	31.63 \rightarrow 35.95
	$\sin^2 \theta_{23}$	$0.561^{+0.012}_{-0.015}$	0.430 \rightarrow 0.596	$0.562^{+0.012}_{-0.015}$	0.437 \rightarrow 0.597
	$\theta_{23}/^\circ$	$48.5^{+0.7}_{-0.9}$	41.0 \rightarrow 50.5	$48.6^{+0.7}_{-0.9}$	41.4 \rightarrow 50.6
	$\sin^2 \theta_{13}$	$0.02195^{+0.00054}_{-0.00058}$	0.02023 \rightarrow 0.02376	$0.02224^{+0.00056}_{-0.00057}$	0.02053 \rightarrow 0.02397
	$\theta_{13}/^\circ$	$8.52^{+0.11}_{-0.11}$	8.18 \rightarrow 8.87	$8.58^{+0.11}_{-0.11}$	8.24 \rightarrow 8.91
	$\delta_{\text{CP}}/^\circ$	177^{+19}_{-20}	96 \rightarrow 422	285^{+25}_{-28}	201 \rightarrow 348
	$\frac{\Delta m_{21}^2}{10^{-5} \text{ eV}^2}$	$7.49^{+0.19}_{-0.19}$	6.92 \rightarrow 8.05	$7.49^{+0.19}_{-0.19}$	6.92 \rightarrow 8.05
	$\frac{\Delta m_{3\ell}^2}{10^{-3} \text{ eV}^2}$	$+2.534^{+0.025}_{-0.023}$	+2.463 \rightarrow +2.606	$-2.510^{+0.024}_{-0.025}$	-2.584 \rightarrow -2.438
	IC24 with SK atmospheric data	$\sin^2 \theta_{12}$	$0.308^{+0.012}_{-0.011}$	0.275 \rightarrow 0.345	$0.308^{+0.012}_{-0.011}$
$\theta_{12}/^\circ$		$33.68^{+0.73}_{-0.70}$	31.63 \rightarrow 35.95	$33.68^{+0.73}_{-0.70}$	31.63 \rightarrow 35.95
$\sin^2 \theta_{23}$		$0.470^{+0.017}_{-0.013}$	0.435 \rightarrow 0.585	$0.550^{+0.012}_{-0.015}$	0.440 \rightarrow 0.584
$\theta_{23}/^\circ$		$43.3^{+1.0}_{-0.8}$	41.3 \rightarrow 49.9	$47.9^{+0.7}_{-0.9}$	41.5 \rightarrow 49.8
$\sin^2 \theta_{13}$		$0.02215^{+0.00056}_{-0.00058}$	0.02030 \rightarrow 0.02388	$0.02231^{+0.00056}_{-0.00056}$	0.02060 \rightarrow 0.02409
$\theta_{13}/^\circ$		$8.56^{+0.11}_{-0.11}$	8.19 \rightarrow 8.89	$8.59^{+0.11}_{-0.11}$	8.25 \rightarrow 8.93
$\delta_{\text{CP}}/^\circ$		212^{+26}_{-41}	124 \rightarrow 364	274^{+22}_{-25}	201 \rightarrow 335
$\frac{\Delta m_{21}^2}{10^{-5} \text{ eV}^2}$		$7.49^{+0.19}_{-0.19}$	6.92 \rightarrow 8.05	$7.49^{+0.19}_{-0.19}$	6.92 \rightarrow 8.05
$\frac{\Delta m_{3\ell}^2}{10^{-3} \text{ eV}^2}$		$+2.513^{+0.021}_{-0.019}$	+2.451 \rightarrow +2.578	$-2.484^{+0.020}_{-0.020}$	-2.547 \rightarrow -2.421

Table 1. Three-flavor oscillation parameters from our fit to global data for the two variants of the analysis described in the text. The numbers in the 1st (2nd) column are obtained assuming NO (IO), *i.e.*, relative to the respective local minimum. Note that $\Delta m_{3\ell}^2 \equiv \Delta m_{31}^2 > 0$ for NO and $\Delta m_{3\ell}^2 \equiv \Delta m_{32}^2 < 0$ for IO.

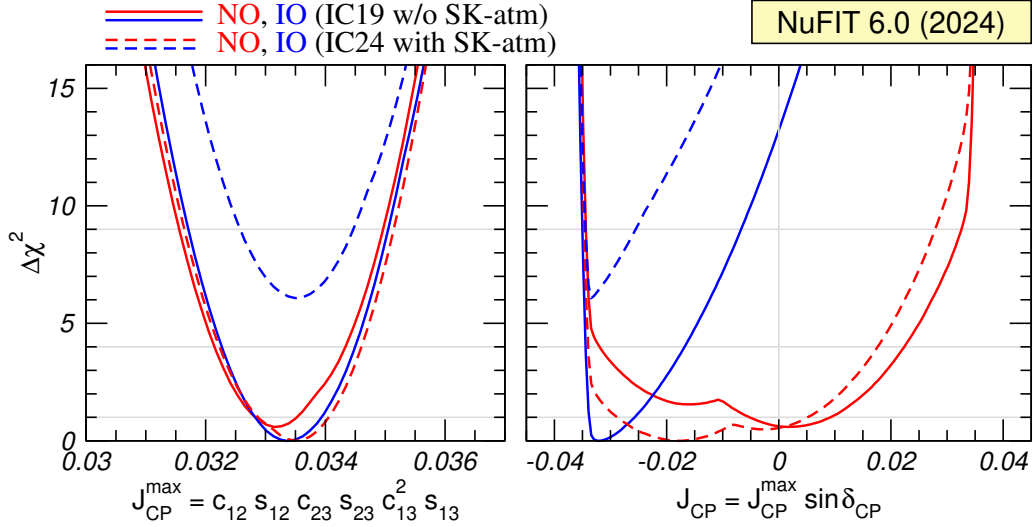


Figure 3. Dependence of the global $\Delta\chi^2$ function on the Jarlskog invariant. The red (blue) curves are for NO (IO). Solid (dashed) curves are for the «IC19 w/o SK-atm» («IC24 with SK-atm») $\Delta\chi^2$.

We quantify the presence of leptonic CP violation in neutrino propagation in vacuum in a convention-independent form in terms of the leptonic Jarlskog invariant [34]:

$$\begin{aligned}
 J_{\text{CP}} &\equiv \text{Im} [U_{\alpha i} U_{\alpha j}^* U_{\beta i}^* U_{\beta j}] \\
 &\equiv J_{\text{CP}}^{\text{max}} \sin \delta_{\text{CP}} = \cos \theta_{12} \sin \theta_{12} \cos \theta_{23} \sin \theta_{23} \cos^2 \theta_{13} \sin \theta_{13} \sin \delta_{\text{CP}} .
 \end{aligned}
 \tag{2.5}$$

Its present determination is shown in Fig. 3, from which we read its maximum value

$$J_{\text{CP}}^{\text{max}} = 0.0333 \pm 0.0007 (\pm 0.0017) .
 \tag{2.6}$$

at 1σ (3σ) for both orderings. J_{CP} is totally analogous to the invariant introduced in Ref. [35] for the description of CP-violating effects in the quark sector, presently determined to be $J_{\text{CP}}^{\text{quarks}} = (3.12_{-0.12}^{+0.13}) \times 10^{-5}$ [36].

Figure 3 also shows that in NO the best-fit value $J_{\text{CP}}^{\text{best}} = 0.0017 (-0.018)$ (where the value in parenthesis corresponds to the analysis with IC24 and SK-atm) is only favored over CP conservation $J_{\text{CP}} = 0$ with $\Delta\chi^2 = 0.02$ (0.55). In contrast, in IO CP conservation is disfavored with respect to $J_{\text{CP}}^{\text{best}} = -0.032$ with $\Delta\chi^2 = 13$ (16), which corresponds to 3.6σ (4σ) when evaluated for 1 dof.

3 Status of neutrino mass ordering, leptonic CP violation, and θ_{23}

3.1 Updates from T2K and NOvA

We start by discussing the implications of the latest data from the T2K and NOvA long-baseline accelerator experiments, presented at the Neutrino 2024 conference. Although our analysis includes the full spectral information provided by the collaborations, qualitative understanding of the results can be obtained from the study of the total number of events in the different appearance samples. To this end, we show in Fig. 4 the predicted number

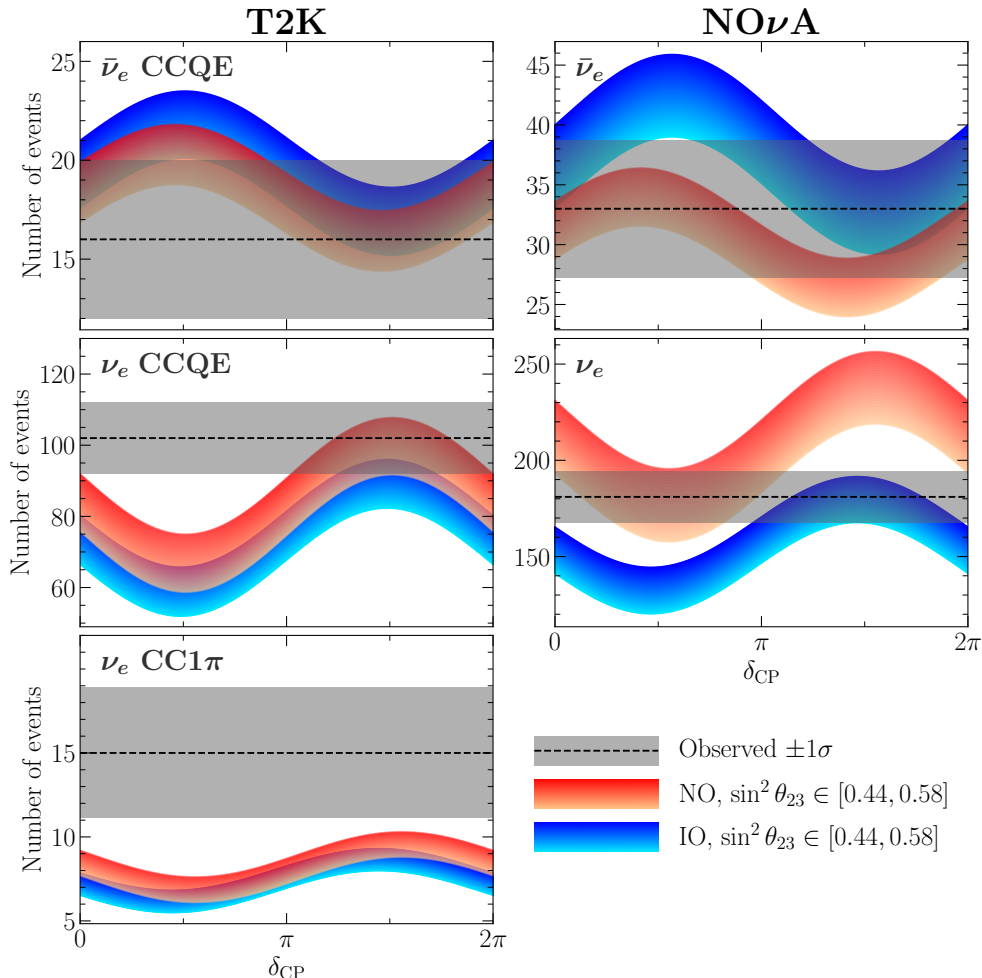


Figure 4. Predicted number of events as a function of δ_{CP} for the T2K (left) and NOvA (right) appearance data sets. $\sin^2 \theta_{23}$ varies between 0.44 and 0.58, where the lower-light (upper-dark) bound of the colored bands corresponds to 0.44 (0.58). Red (blue) bands correspond to NO (IO). For the other oscillation parameters we have adopted $\sin^2 \theta_{13} = 0.0222$, $|\Delta m_{3\ell}^2| = 2.5 \times 10^{-3} \text{ eV}^2$, $\sin^2 \theta_{12} = 0.32$, $\Delta m_{21}^2 = 7.5 \times 10^{-5} \text{ eV}^2$. The horizontal dashed lines show the observed number of events, with the $\pm 1\sigma$ statistical error indicated by the gray shaded band.

of events for these samples as a function of δ_{CP} , for varying values of $\sin^2 \theta_{23}$, as well as the mass ordering, compared to the observations.

The predictions in Fig. 4 are calculated using our simulations of the experiments, that include numerically-computed oscillation probabilities. However, the general behaviour of the curves is well-described by the approximate expressions derived in Refs. [25, 37]. These expand the relevant oscillation probabilities in the small parameters $\sin \theta_{13}$, $\Delta m_{21}^2 L/E_\nu$, and $A \equiv |2E_\nu V/\Delta m_{3\ell}^2|$ (where L is the baseline, E_ν the neutrino energy and V the effective matter potential [38]), resulting in the following expressions for the expected number of events:

$$N_{\nu_e} \approx \mathcal{N}_\nu \left[2s_{23}^2(1 + 2oA) - C' \sin \delta_{\text{CP}}(1 + oA) \right], \quad (3.1)$$

	T2K (ν)			T2K ($\bar{\nu}$)	NOvA (ν)	NOvA ($\bar{\nu}$)
	CCQE	CC1 π	Sum			
\mathcal{N}	54	5	59	13	104	23
N_{obs}	102	15	117	16	181	33
$N_{\text{obs}} - N_{\text{bck}}$	81.6	12.5	94.2	10	117.3	19
$r = \frac{N_{\text{obs}} - N_{\text{bck}}}{\mathcal{N}}$	1.5 (1.6)	2.5 (2.4)	1.59 (1.65)	0.77 (0.61)	1.13 (1.14)	0.83 (0.83)

Table 2. Normalization coefficients \mathcal{N}_ν and $\mathcal{N}_{\bar{\nu}}$ in eqs. (3.1) and (3.2) for approximations used to qualitatively describe the appearance event samples for T2K and NOvA. Numbers in parentheses are the corresponding values for the data set used for NuFIT 5.0.

$$N_{\bar{\nu}_e} \approx \mathcal{N}_{\bar{\nu}} [2s_{23}^2(1 - 2oA) + C' \sin \delta_{\text{CP}}(1 - oA)] , \quad (3.2)$$

where $o \equiv \text{sgn}(\Delta m_{3\ell}^2)$. For T2K the mean neutrino energy gives $A \approx 0.05$, whereas for NOvA we find that the approximation works best with the *empirical* value of $A = 0.1$. Furthermore, taking all of the well-determined parameters θ_{13} , θ_{12} , Δm_{21}^2 , $|\Delta m_{3\ell}^2|$ at their global best-fit points, we obtain numerically $C' \approx 0.28$ with negligible dependence on θ_{23} . The normalization constants $\mathcal{N}_{\nu, \bar{\nu}}$ calculated from our re-analysis of T2K and NOvA are given for the various appearance samples in Table 2, along with the corresponding observed event numbers and expected backgrounds. We can obtain insight on the results of the fit by considering the ratio $r \equiv (N_{\text{obs}} - N_{\text{bck}})/\mathcal{N}$.

From the numbers in the table we observe the following:

- T2K data has $r > 1$ for neutrinos and $r < 1$ for antineutrinos, so the square-bracket in Eq. (3.1) has to be enhanced and the one in Eq. (3.2) suppressed. This can be achieved with $\delta_{\text{CP}} \simeq 3\pi/2$, with a better fit in NO. This preference has been present since the first T2K results on ν_e appearance. As can be seen in the last line of Table 2, although the preference is somewhat weaker in NuFIT 6.0 than it was in NuFIT 5.0, it is still significant; and the strongest observed effect remains in the lower-statistics CC1 π sample.
- NOvA antineutrino results have not changed since NuFIT 5.0. They have $r < 1$ and can be accommodated with either NO and $\delta_{\text{CP}} \simeq \pi/2$, or IO and $\delta_{\text{CP}} \simeq 3\pi/2$, with a slightly better fit in NO.
- NOvA neutrino results have now 60% more statistics than in NuFIT 5.0, and they still result in $r \sim 1$. This can also be accommodated with either NO and $\delta_{\text{CP}} \simeq \pi/2$, or IO and $\delta_{\text{CP}} \simeq 3\pi/2$, totally compatible with the NOvA antineutrino results. Altogether, the results from NOvA only show a very mild preference for NO.
- The favored values of δ_{CP} in NO by T2K and NOvA do not agree. Consequently, the combination of both experiments is better described in IO with $\delta_{\text{CP}} \simeq 3\pi/2$. This was already the case in NuFIT 5.0, and the tendency has strengthened with the updated results.

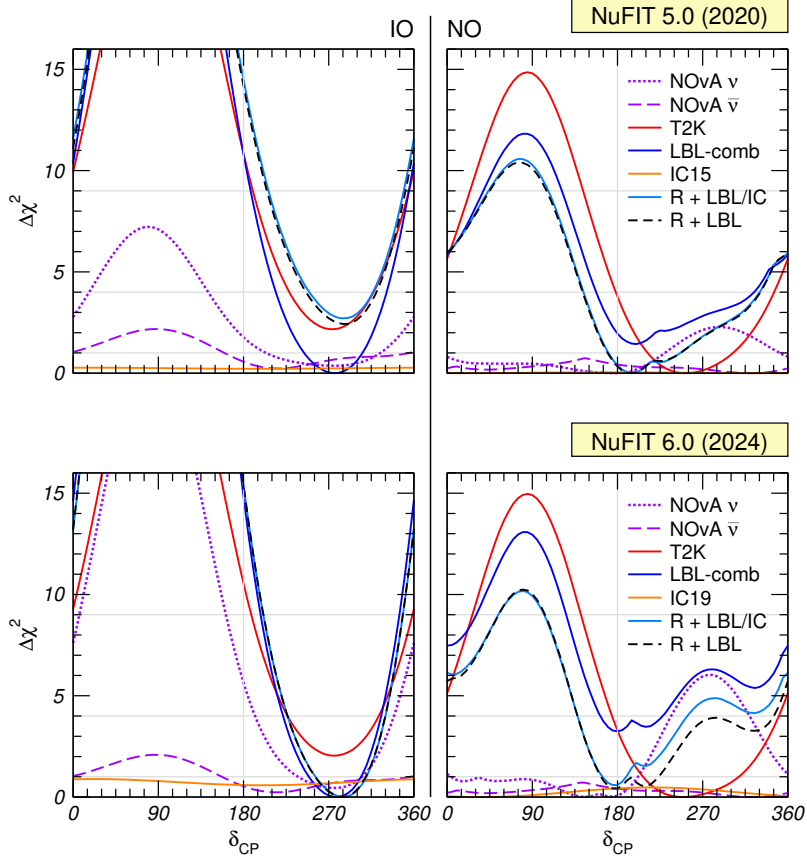


Figure 5. $\Delta\chi^2$ profiles as a function of δ_{CP} for different data sets and combinations as labeled in the figure. In the curves where the reactors R are not included in the combination we have fixed $\sin^2\theta_{13} = 0.0222$ as well as the solar parameters and minimized with respect to θ_{23} and $|\Delta m_{3\ell}^2|$. When the reactors are included θ_{13} is also marginalized. Left (right) panels are for IO (NO) and $\Delta\chi^2$ is shown with respect to the global best-fit point for each curve. Upper panels are for the NuFIT 5.0 data set, whereas lower panels correspond to the current update.

This is further illustrated in Fig. 5, which shows the $\Delta\chi^2$ profiles as a function of δ_{CP} for the LBL experiments T2K and NOvA and their combination (we also add the information from MBL reactors and from the IC atmospheric samples which we independently analyzed in NuFIT 5.0 and NuFIT 6.0, and will discuss in Sec. 3.2). Comparing the curves of T2K and NOvA in the upper and lower panels, we see that the main difference is in the NOvA neutrino results. Just by themselves, they disfavor NO and $\delta_{\text{CP}} \simeq 3\pi/2$ by about 6 units in χ^2 (versus 3 units in NuFIT 5.0), whereas comparing the corresponding curves in the left panels we see that for IO the consistent preference of T2K and NOvA for $\delta_{\text{CP}} \simeq 3\pi/2$ is now statistically more significant. Altogether, this drives the preference of the LBL combination for IO, with $\Delta\chi^2(\text{NO} - \text{IO}) \approx 3.2$ versus 1.5 in NuFIT 5.0.

The two-dimensional regions for T2K and NOvA in the $(\delta_{\text{CP}}, \sin^2\theta_{23})$ plane for fixed θ_{13} are shown in Figure 6. The better consistency for IO is apparent. For NO we find that, unlike in NuFIT 5.0, the 1σ regions do not overlap. The 2-dimensional projections in the

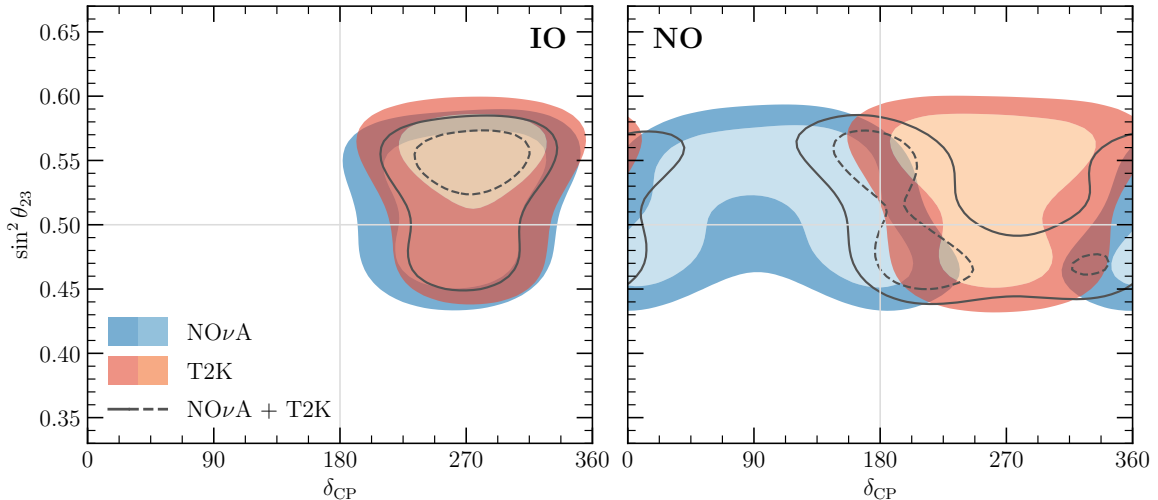


Figure 6. 1σ and 2σ allowed regions (2 dof) for T2K (red shading), NO ν A (blue shading) and their combination (black curves). Contours are defined with respect to the local minimum for IO (left) or NO (right). We fix $\sin^2 \theta_{13} = 0.0222$, $\sin^2 \theta_{12} = 0.31$, $\Delta m_{21}^2 = 7.5 \times 10^{-5} \text{ eV}^2$ and minimize with respect to $|\Delta m_{3\ell}^2|$.

$(\delta_{\text{CP}}, \sin^2 \theta_{23})$ plane from the global analysis of all data are shown in Fig. 7, which resemble to a large extent the features from the combination among T2K and NO ν A discussed above. We observe, in particular, non-trivial correlations between these two parameters and the MO. For IO, the preference for $\delta_{\text{CP}} \simeq 270^\circ$ is highly significant, whereas for NO a more complicated structure in the $(\delta_{\text{CP}}, \sin^2 \theta_{23})$ plane, with several local minima, emerges. The octant degeneracy for θ_{23} is present with $\Delta\chi^2 < 4$ for both mass orderings and both data variants, showing local minima around $\sin^2 \theta_{23} \approx 0.56$ and 0.47 .

An obvious question to address is whether T2K and NO ν A are in tension with each other at a worrisome level. Consistency among different data sets can be quantified with the parameter goodness-of-fit (PG) [39]. For a number N of different data sets i , each depending on n_i model parameters, and globally depending on n_{glob} parameters, it can be shown that the test statistic

$$\chi_{\text{PG}}^2 \equiv \chi_{\text{min, glob}}^2 - \sum_i^N \chi_{\text{min, } i}^2 = \min \left[\sum_i^N \chi_i^2 \right] - \sum_i \chi_{\text{min, } i}^2, \quad (3.3)$$

follows a χ^2 distribution with $n \equiv \sum_i n_i - n_{\text{glob}}$ degrees of freedom [39].

Applying this test to the full NO ν A and T2K samples (including both appearance and disappearance data for neutrinos and antineutrinos) we obtain the values in Table 3. We carry out the analysis separately for each mass ordering, in all cases fixing Δm_{21}^2 and θ_{12} to their best fit. In the results reported in the upper part of the table θ_{13} is varied in the minimization, so $n_{\text{T2K}} = n_{\text{NO}\nu\text{A}} = n_{\text{glob}=\text{T2K}+\text{NO}\nu\text{A}} = 4$ (*i.e.*, $\Delta m_{3\ell}^2$, θ_{23} , δ_{CP} , and θ_{13}). In the lower part θ_{13} is kept fixed to its best fit so $n_{\text{T2K}} = n_{\text{NO}\nu\text{A}} = n_{\text{glob}=\text{T2K}+\text{NO}\nu\text{A}} = 3$. From the table we read that, as expected, agreement is better in IO, where irrespective on θ_{13} the samples are compatible at the 0.5σ level or better. In NO, compatibility arises

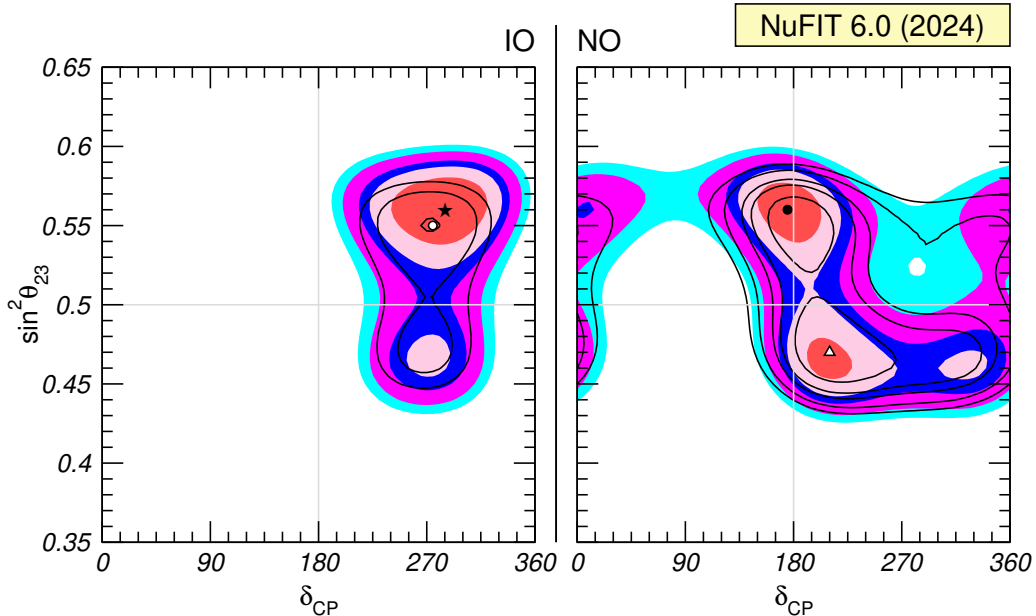


Figure 7. Two-dimensional projection of the allowed six-dimensional region from global data in the plane of $(\delta_{\text{CP}}, \sin^2 \theta_{23})$ for IO (left) and NO (right) after minimization with respect to the undisplayed parameters. Regions for both orderings are defined with respect to the global best-fit point. The different contours correspond to 1σ , 90%, 2σ , 99%, 3σ CL (2 dof). Colored regions (black contours) correspond to the variant with IC19 and without SK-atm (with IC24 and with SK-atm).

at 1.7σ (2.0σ) for free (fixed) θ_{13} . This is to be compared with the NuFIT 5.0 results of 1.4σ (1.7σ) respectively. We conclude that the tension between T2K and NOvA in NO has slightly strengthened with the new results, reaching at most the 2σ level.

3.2 Effects from $\nu_\mu/\bar{\nu}_\mu$ versus $\bar{\nu}_e$ disappearance

Figure 8 shows the combined determination of the parameters $\sin^2 \theta_{23}$, $\sin^2 \theta_{13}$, and $\Delta m_{3\ell}^2$ by the interplay of different data samples, namely $\nu_\mu/\bar{\nu}_\mu$ disappearance from long-baseline accelerator and atmospheric neutrino data (left panel) and $\bar{\nu}_e$ disappearance from medium baseline reactor experiments (right panel). We observe significant synergy from the combination of different data sets (global regions are clearly smaller than individual ones) as well as appealing consistency. This is also reflected by the many compatibility tests reported in Table 3, which all show very good consistency typically well below 2σ .

As in previous analyses, the combination of ν_μ and $\bar{\nu}_\mu$ disappearance data (dominated by LBL accelerator experiments) with $\bar{\nu}_e$ disappearance from reactors provides complementary information, which is especially relevant for the MO discrimination [40, 41]. In short, the effective mass-squared difference relevant for each survival probability depends on the mass ordering, so a global combination allows in principle to determine it. This effect can be seen in 1-dimensional χ^2 projections on the parameter $\Delta m_{3\ell}^2$, as shown in Fig. 9.

In the upper panels we show the profiles for various individual data sets. We observe that, individually, the considered data are either insensitive to the MO ($\Delta\chi^2 < 1$) or show

Data sets	Normal Ordering			Inverted Ordering		
	χ_{PG}^2/n	p -value	$\#\sigma$	χ_{PG}^2/n	p -value	$\#\sigma$
T2K vs NOvA	7.9/4	0.093	1.7	2.3/4	0.67	0.42
T2K vs React	0.23/2	0.89	0.14	1.7/2	0.43	0.79
NOvA vs React	1.1/2	0.58	0.56	4.3/2	0.12	1.6
T2K vs NOvA vs React	8.6/6	0.20	1.3	6.0/6	0.42	0.80
(T2K & NOvA) vs React	0.76/2	0.68	0.41	3.4/2	0.18	1.3
T2K vs IC19	2.7/4	0.61	0.51	1.2/4	0.88	0.15
NOvA vs IC19	3.3/4	0.51	0.66	2.3/4	0.68	0.41
Reac vs IC19	2.1/2	0.35	0.93	0.88/2	0.64	0.84
NOvA vs T2K vs IC19	11/8	0.20	1.3	4.3/8	0.83	0.21
NOvA vs T2K vs React vs IC19	11.5/10	0.33	0.96	7.2/10	0.71	0.38
T2K vs NOvA	8.0/3	0.045	2.0	1.8/3	0.61	0.50
T2K vs NOvA vs React	8.3/4	0.081	1.7	4.1/4	0.39	0.85
(T2K & NOvA) vs React	0.25/1	0.62	0.50	2.0/1	0.16	1.4
T2K vs IC19	0.72/3	0.86	0.16	0.2/3	0.98	0.028
NOvA vs IC19	1.5/3	0.68	0.41	1.0/3	0.80	0.25
NOvA vs T2K vs IC19	9.3/6	0.16	1.4	2.4/6	0.88	0.15
NOvA vs T2K vs React vs IC19	9.4/7	0.22	1.2	4.5/7	0.72	0.36
NOvA vs T2K vs IC24	9.5/6	0.15	1.4	4.4/6	0.62	0.49
NOvA vs T2K vs React vs IC24	10/7	0.19	1.3	8.2/7	0.27	1.1

Table 3. Consistency test among different data sets, shown in the first column, assuming either normal or inverted ordering. “React” includes Daya-Bay, RENO and Double-Chooz. In the analyses above the horizontal line, θ_{13} is a free parameter, whereas below the line we have fixed $\sin^2 \theta_{13} = 0.0222$. See text for more details.

a slight preference for NO. The only exception is the LBL/IC combination, which prefers IO due to the T2K/NOvA tension discussed above. However, by comparing the LBL and reactor results, we observe that the determination of $|\Delta m_{3\ell}^2|$ is in better agreement for NO than for IO. Hence, combining reactor and LBL data (bottom-left panels) increases the value of $\Delta\chi_{\text{IO,NO}}^2 \equiv \chi_{\text{min,IO}}^2 - \chi_{\text{min,NO}}^2$ in favor of NO. As a result, the preference for IO from the T2K/NOvA combination (dominated by appearance data) is nearly exactly compensated by the effects of disappearance data in the LBL/reactor combination, leading to a global result of $\Delta\chi_{\text{IO,NO}}^2 = -0.6$.

The preference for NO from the accelerator/reactor combination is also visible in the PG tests in Table 3, by considering the consistency among the combined T2K & NOvA sample and reactors. For both θ_{13} free and fixed, there is slightly better compatibility for NO than IO (although even for IO consistency is very good, 1.3σ or 1.4σ). This preference is only visible when combining T2K and NOvA *before* testing the consistency (*i.e.*, the rows labeled «(T2K & NOvA) vs React»). Otherwise, if they are kept separate (*i.e.*, the rows labeled «T2K vs NOvA vs React») the opposite trend from the combination among T2K and NOvA appearance samples compensates for the tendency from disappearance data.

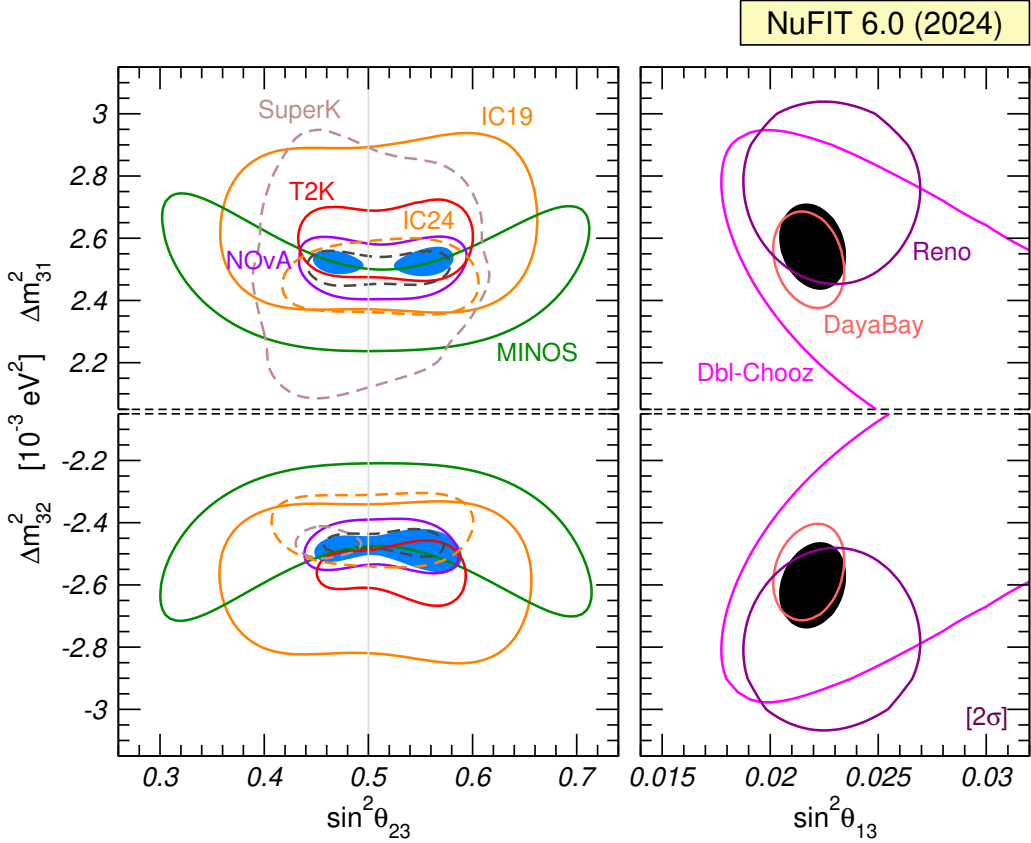


Figure 8. Confidence regions at 95.45% CL (2 dof) in the plane of $\sin^2 \theta_{23}$ ($\sin^2 \theta_{13}$) and $\Delta m_{3\ell}^2$ in the left (right) panels. For the left panels we use both appearance and disappearance data from MINOS (green), NOvA (purple) and T2K (red), as well as atmospheric data from IC (orange) and Super-Kamiokande (light-brown); the colored region corresponds to the combination of these accelerator data with IC19, whereas the black-dashed contour corresponds to the combination with IC24 and Super-Kamiokande. A prior on θ_{13} is included to account for the reactor constraint. The right panels show regions using data from Daya-Bay (pink), Double-Chooz (magenta), RENO (violet), and their combination (black regions). In all panels solar, KamLAND and SNO+ data are included to constrain Δm_{21}^2 and θ_{12} . Contours are defined with respect to the global minimum of the two orderings for each data set.

In the right half of Fig. 9, we show the impact of the different IceCube data samples. It is clear from the figure that the IC19 3-year data sample [19, 20] plays very little role in the ν_μ/ν_e disappearance complementarity due to its relatively weak constraint on $|\Delta m_{3\ell}^2|$. However, when combining the IC24 χ^2 table corresponding to 9.3 years of data [23, 24] with reactor data, this complementarity [42] already provides a preference for NO, with $\Delta\chi_{\text{IO,NO}}^2 \approx 4.5$. The result is entirely driven by the $|\Delta m_{3\ell}^2|$ determination, as the χ^2 tables provided by the collaboration contain no information on the IceCube MO sensitivity (they only provide relative $\Delta\chi^2$ values with respect to the best fit *in each ordering*). Let us remark, however, that the $\Delta\chi_{\text{IO,NO}}^2 = 4.5$ contribution from combining IC24 and reactors does not simply add up to the value $\Delta\chi_{\text{IO,NO}}^2 = -0.6$ from combining LBL and reactors.

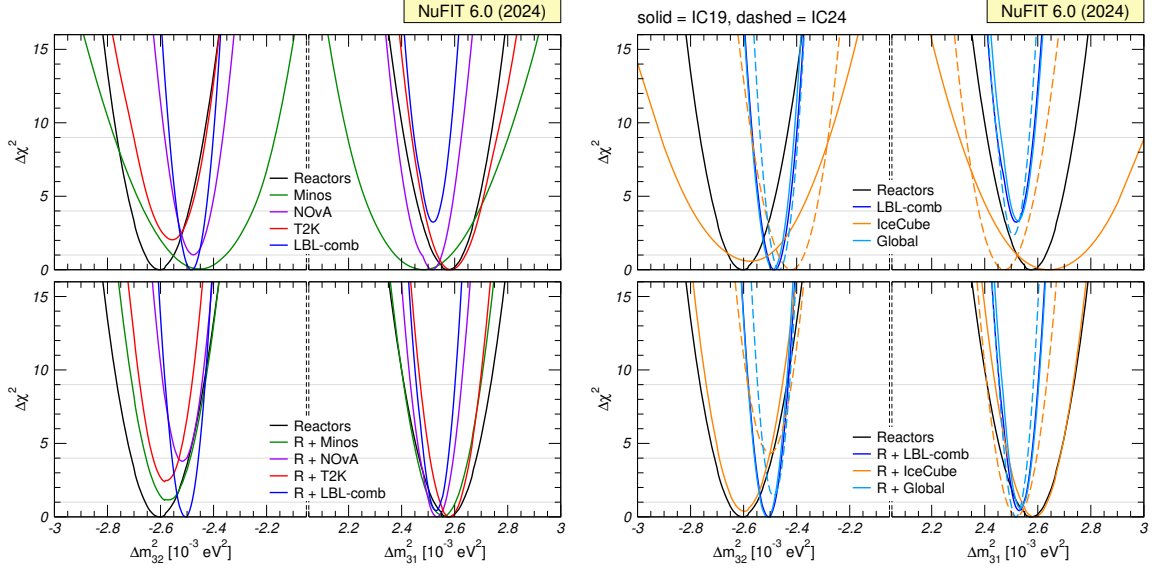


Figure 9. $\Delta\chi^2$ profiles as a function of $\Delta m_{3\ell}^2$ for different data sets and combinations as labeled in the figures. In the curves where the reactors R are not included in the combination we have fixed $\sin^2 \theta_{13} = 0.0222$ as well as the solar parameters and minimized with respect to θ_{23} and δ_{CP} . When the reactors are included θ_{13} is also marginalized. $\Delta\chi^2$ is shown with respect to the global best-fit point (IO or NO) for each curve. The left set of panels visualizes the reactor/LBL combination, whereas in the right set of panels we are illustrating the impact of the IC19 or IC24 data sets.

Instead, combining LBL and IC24 leads to a shift in $|\Delta m_{3\ell}^2|$ that, when adding reactor data, leads to $\Delta\chi_{IO,NO}^2 \approx 1.5$.

Different to the IC24 data table, the latest Super-Kamiokande atmospheric data [22] alone shows a preference for NO with $\Delta\chi_{IO,NO}^2 \approx 5.7$. We note, however, that this result seems to emerge from a large statistical fluctuation. Indeed, the probability of obtaining the data is relatively low for both mass orderings, and considering the distribution of the relevant test statistic, the SK collaboration determines a preference for NO over IO at the 92.3% CL [21]. When combining the IC24 and SK atmospheric neutrino χ^2 tables with our global fit of the remaining data, we find an overall preference for NO with $\Delta\chi_{IO,NO}^2 \approx 6.1$, see Sec. 2.

3.3 Sensitivity to the neutrino mass ordering

Given the different trends among several determinations of the mass ordering, we now study in more detail the sensitivity of current global data to it. To do so, we follow the methodology in Ref. [43]. As customary, a useful test statistic for this purpose is the χ^2 difference among the best-fit points for the two orderings. Following Ref. [43], we denote it in this Section as T ,

$$T \equiv \Delta\chi_{IO,NO}^2 \equiv \chi_{\min,IO}^2 - \chi_{\min,NO}^2. \quad (3.4)$$

Hence, positive values of T favor NO, and negative values favor IO. As shown in refs. [43, 44], under certain conditions T will follow a Gaussian distribution with mean $\pm T_0$ and standard deviation $2\sqrt{T_0}$, where T_0 is obtained as follows. If $p_i(o, \theta)$ is the expected number of events

in bin i (where $o \in \{\text{NO}, \text{IO}\}$ is the mass ordering and θ are the remaining oscillation parameters), d_i is the observed number of events in that bin, and the global χ^2 is given by $\chi^2 = \chi^2[p_i(o, \theta); d_i]$, then

$$\begin{aligned} T_0^{\text{NO}} &\equiv \min_{\theta} \left\{ \chi^2 [p_i(\text{IO}, \theta); p_i(\text{NO}, \theta^{\text{true}})] \right\}, \\ T_0^{\text{IO}} &\equiv \min_{\theta} \left\{ \chi^2 [p_i(\text{NO}, \theta); p_i(\text{IO}, \theta^{\text{true}})] \right\}. \end{aligned} \quad (3.5)$$

That is, T_0 is determined by replacing the data by the prediction for the opposite mass ordering, given some assumed true values of oscillation parameters. Defined this way, T_0^o is always positive. Hence, for true NO (IO) the expected value of T is $+T_0^{\text{NO}}$ ($-T_0^{\text{IO}}$). The conditions under which the aforementioned Gaussian approximation holds are discussed in detail in the Appendix of Ref. [43], and they are similar to the conditions for Wilks' theorem. In the following, we will study the results of the global fit under the assumption that T is indeed Gaussian-distributed. In addition, the values of T_0^o defined in Eq. (3.5) depend on the (unknown) true values of the oscillation parameters θ^{true} . In the following, we will take them to be the best-fit points of our analysis as given in Table 1; we comment on this assumption in Appendix C.

This analysis cannot be carried out for the atmospheric neutrino data samples IC24 and Super-Kamiokande, which are included in our global fit as numerical χ^2 tables. Therefore, in what follows we only consider the data sample denoted by «IC19 w/o SK-atm». ¹ For the global data combination, we find

$$T_0^{\text{NO}} = 6.47, \quad T_0^{\text{IO}} = 4.85. \quad (3.6)$$

The corresponding normal distributions for T are shown in the bottom panel of Fig. 10. For an observed value T_{obs} , we compute the p -value for a given mass ordering as usual: the p -value for IO (NO) is the probability to obtain a value of T larger (smaller) than T_{obs} if the true ordering is IO (NO). Given the observed value for the global fit, $T_{\text{obs}} = -0.6$, the corresponding p -values are indicated by shaded areas in the lower panel of Fig. 10 and can be read off from the intersection of the red and blue curves with the T_{obs} value in the upper panel:

$$\begin{aligned} \text{NO: } p_{\text{NO}} &= 8.2\%, \quad 91.8\% \text{ CL}, \quad 1.7\sigma, \\ \text{IO: } p_{\text{IO}} &= 16.7\%, \quad 83.3\% \text{ CL}, \quad 1.4\sigma. \end{aligned} \quad (3.7)$$

As expected for $|T_{\text{obs}}| < 1$, the p -values for both orderings are similar and we cannot significantly favor one over the other. Indeed, none of the orderings can be rejected at relevant significance; we obtain p -values below 2σ for both orderings, with a slightly smaller p -value for NO due to the negative value of T_{obs} .

Given the distribution for T , we can estimate the sensitivity of the considered data set. In particular, the median sensitivity is obtained by assuming that T_{obs} is given by the mean value of T for a given mass ordering. Hence, the median p -value is given by the intersection

¹This is unfortunate, as the IC24 and SK samples provide relevant sensitivity to the MO (see above).

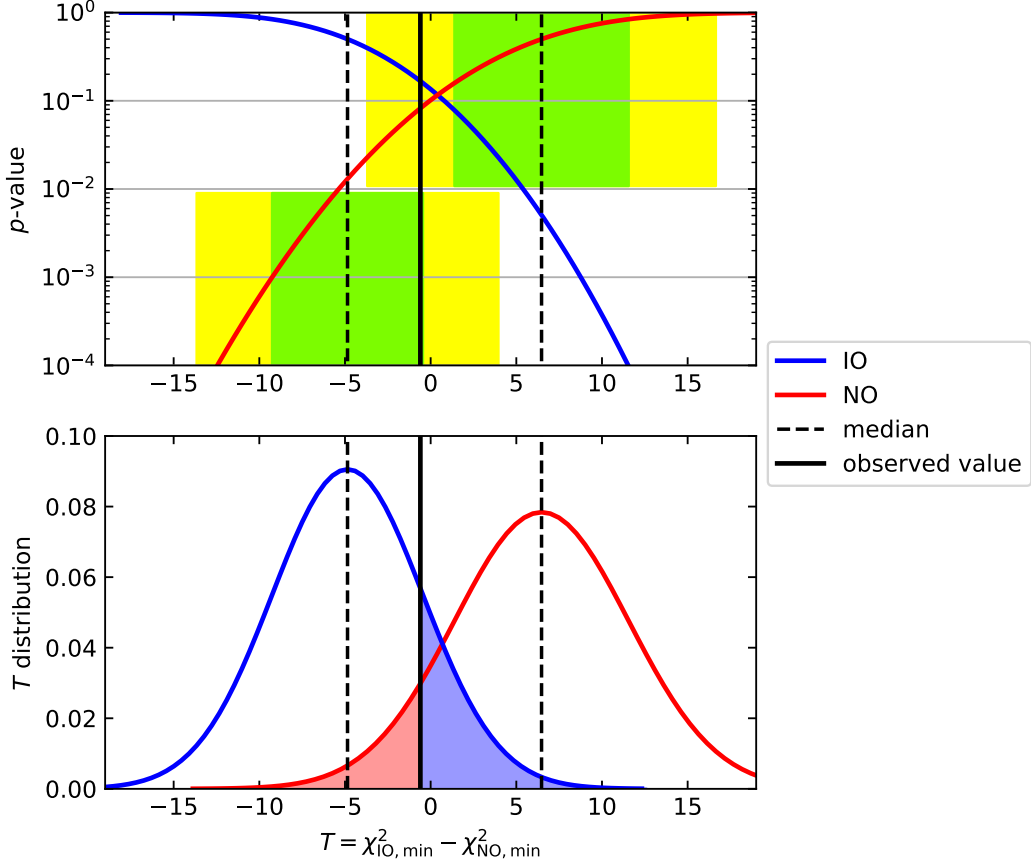


Figure 10. p -values (top) and distributions (bottom) for the test statistic $T = \chi_{\text{IO},\text{min}}^2 - \chi_{\text{NO},\text{min}}^2$ corresponding to the «IC19 w/o SK-atm» analysis, assuming true NO (red) or true IO (blue). The observed value $T_{\text{obs}} = -0.6$ is shown by the solid vertical black line. The corresponding median values are shown by the dashed vertical lines. The green and yellow bands in the top panel—vertically displaced to avoid graphical overlap—correspond to the 1σ and 2σ intervals for T assuming NO (upwards displaced bands) and IO (downwards displaced bands).

of the dashed lines with the corresponding red or blue curves in the top panel of Fig. 10,

$$\begin{aligned}
 \text{NO: } p_{\text{NO}}^{\text{med}} &= 1.3\%, \quad 98.7\% \text{ CL}, \quad 2.5\sigma, \\
 \text{IO: } p_{\text{IO}}^{\text{med}} &= 0.51\%, \quad 99.49\% \text{ CL}, \quad 2.8\sigma.
 \end{aligned}
 \tag{3.8}$$

We conclude that current data has a nominal sensitivity above 2.5σ to the mass ordering. The weak rejection we obtain for both orderings is a result of the opposite trends in the data discussed in previous subsections, resulting in an observed value for T_{obs} right in between the peaks of the distributions. A natural question is how unlikely this result is. To assess it, we show in the top panel of Fig. 10 the intervals where T_{obs} is expected to lie with probability of 68.27% (green) and 95.45% (yellow) for the two mass orderings. We see that the obtained value $T_{\text{obs}} = -0.6$ is not particularly unlikely for both orderings, being located within the 1σ (2σ) ranges for IO (NO).

4 Updates in the “12” sector

The analyses of the solar experiments and of reactor experiments at $\mathcal{O}(100\text{ km})$ distance (which we refer to as LBL reactor experiments) give the dominant contribution to the determination of Δm_{21}^2 and θ_{12} . We show in Fig. 11 the present determination of these parameters from the global solar analysis in comparison with that of LBL reactor data.

In the solar neutrino sector, new data included since NuFIT 5.0 are the full day-night spectrum from the phase-IV of Super-Kamiokande [45], and the final spectra from Borexino phases-II [12] and III [13]. As for the predictions required for the solar neutrino analysis, the main update is that we have employed the new generation of Standard Solar Models [10]. In brief, for the last two decades solar modeling has suffered from the so-called solar composition problem, associated with the choice of the input for heavy element abundances. They were either taken from the older results from Ref. [46] (GS98), which implied a higher metallicity and predicted solar properties in good agreement with helioseismology observations, or the newer abundances (obtained with more modern methodology and techniques) summarized in Ref. [47] (AGSS09), which implied a lower metallicity and did not agree with helioseismology. Consequently, two different sets of Standard Solar Models were built, each based on the corresponding set of solar abundances [48–50]. On this front, an update of the AGSS09 results was presented by the same group (AAG21) [51], leading only to a slight increase of the solar metallicity. On top of that, a new set of results (MB22) [52] — based on similar methodologies and techniques but with different atomic input data for the critical oxygen lines, among other differences — led to a substantial change in solar element abundances with respect to AGSS09, more in agreement with those from GS98. Therefore, the models built following MB22 provide a good description of helioseismology results.

In Fig. 11 we show the present determination of Δm_{21}^2 and θ_{12} from the global solar analysis performed with the two extreme versions of the Standard Solar Model, namely the one based on the AAG21 abundances and the one based on the MB22-met abundances. From the figure, we see that the determination of the parameters is robust under the changes in the modeling, though the allowed ranges — particularly at higher CL — is different for the two models. In this respect, it is important to point out that the latest Standard-Solar-Model-independent determination of the solar fluxes performed in Ref. [53] shows better agreement with the predictions of the MB22 models. For this reason, we adopt the MB22 as the reference model employed for the results reported in NuFIT 6.0.

In what respects the relevant data from reactor experiments, we have updated the antineutrino fluxes used for the predictions to the latest Daya-Bay measurements [14]. Furthermore, we have included in the fit our analysis of the first results reported by the SNO+ collaboration, which combines the 114 ton-yr of data gathered during the partial-fill phase reported in Ref. [15] and the first 286 ton-yr of data of the full-fill phase presented at Neutrino 2024 [16, 17]. We show in the right panel of Fig. 11 the $\Delta\chi^2$ dependence on Δm_{21}^2 after marginalizing over θ_{12} (fixing $\sin^2\theta_{13} = 0.0222$). Although the precision of SNO+ is still far from that of KamLAND, it is interesting to note that its present best fit is slightly higher than that of KamLAND, though the impact in the combination is

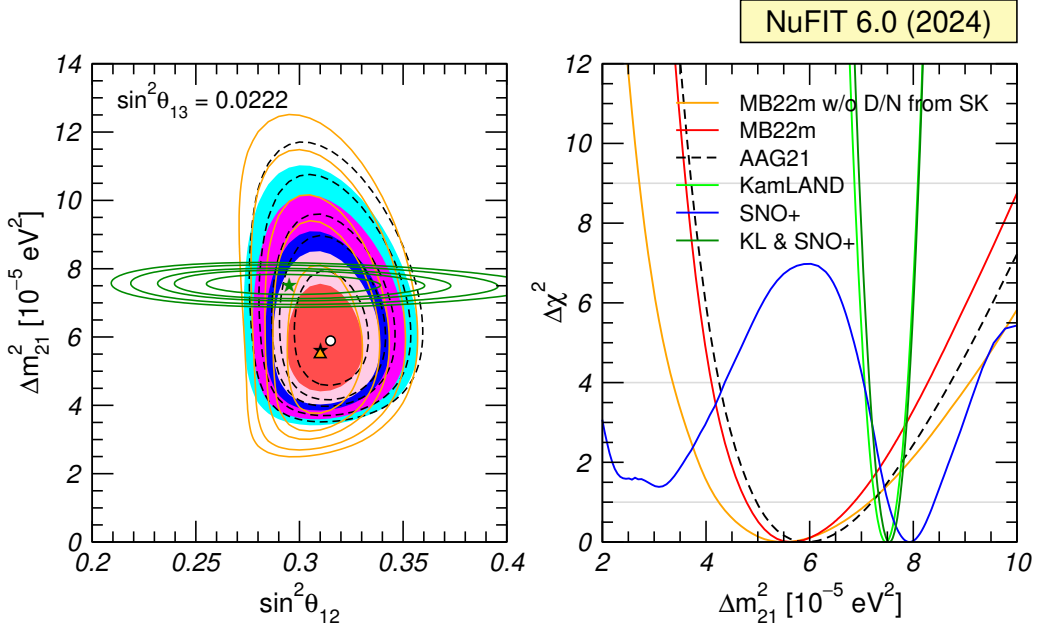


Figure 11. Left: Allowed parameter regions (at 1σ , 90%, 2σ , 99%, and 3σ CL for 2 dof) from the combined analysis of solar data for MB22-met model (full regions with best fit marked by black star) and AAG21 model (dashed void contours with best fit marked by a white dot), and for the analysis of the combination of KamLAND and SNO+ data (solid green contours with best fit marked by a green star) for fixed $\sin^2 \theta_{13} = 0.0222$. For comparison we also show as orange contours the results obtained with the MB22-met model without including the results of the day-night variation in SK. Right: $\Delta\chi^2$ dependence on Δm_{21}^2 for the same four analyses after marginalizing over θ_{12} . In addition we show separately the results from KamLAND and SNO+.

still very marginal as seen in the figure. Nevertheless, the results from SNO+ and the expected statistics increase will be interesting to follow due to their potential impact in the tension/agreement between the solar and reactor determination of Δm_{21}^2 . In that respect, from the figure we read that the present best-fit value of Δm_{21}^2 for the reactor results lies at $\Delta\chi_{\text{solar,MB22}}^2 = 2.5$, which represent a slight increase over the $\Delta\chi_{\text{solar,GS98}}^2 = 1.3$ reported in NuFIT 5.0. For comparison, we show in orange the results of the solar analysis without including the Day-Night variation information from Super-Kamiokande. As seen in the figure, removing that information brings the agreement further down to $\Delta\chi^2 \sim 1.5$. Altogether the latest updates lead to very mild changes in the determination of “solar” parameters ($\sim 1\%$ shift up in the best-fit value and $\sim 10\%$ improvement in the precision) reassuring the robustness of the results.

5 Projections on neutrino mass scale observables

Because of its quantum-interference nature, mass-induced flavor oscillations are sensitive to the phase differences induced by the mass-squared splittings Δm_{ij}^2 and to misalignment between the detection and propagation eigenstates, *i.e.*, to the leptonic mixing matrix elements $U_{\alpha j}$. They are, however, insensitive to overall shifts of the energy levels, and hence

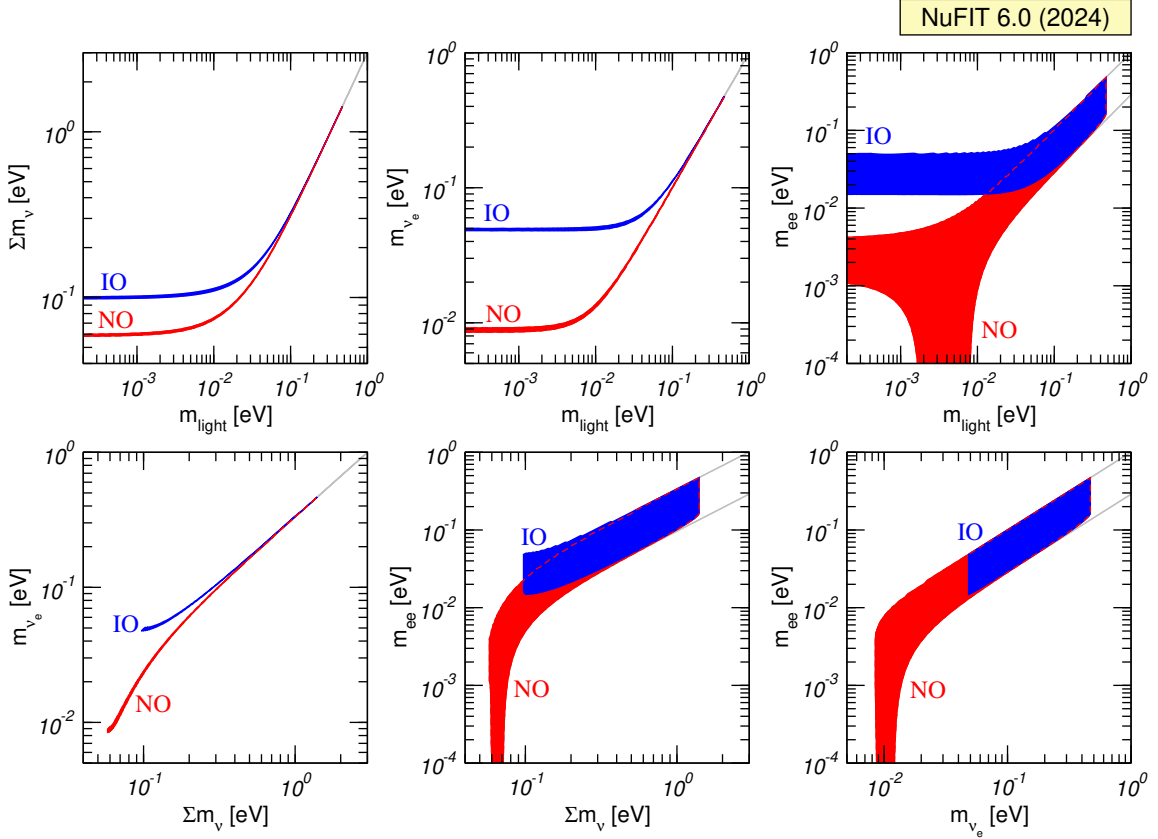


Figure 12. Upper: 95% CL allowed ranges of the three probes of the absolute neutrino mass Σm_ν , m_{ν_e} , m_{ee} as a function of the mass of the lightest neutrino obtained from projecting the results of the global analysis of oscillation data. The regions are defined with respect to the minimum for each ordering. Lower: Corresponding 95% CL allowed regions (for 2 dof) in the planes $(m_{\nu_e}, \Sigma m_\nu)$, $(m_{ee}, \Sigma m_\nu)$, and (m_{ν_e}, m_{ee}) .

they cannot provide information on the absolute mass scale of the neutrinos other than the obvious lower bound on the masses of the heaviest states involved in the oscillations.

The most model-independent information on the neutrino mass, rather than on mass differences, is obtained from kinematic studies of reactions in which a neutrino or an antineutrino is involved. In the presence of mixing, the most relevant constraint comes from the study of the end point ($E \sim E_0$) of the electron spectrum in Tritium beta decay ${}^3\text{H} \rightarrow {}^3\text{He} + e^- + \bar{\nu}_e$. This spectrum can be effectively described by a single parameter, m_{ν_e} , if for all neutrino states $E_0 - E \gg m_i$:

$$m_{\nu_e}^2 \equiv \frac{\sum_i m_i^2 |U_{ei}|^2}{\sum_i |U_{ei}|^2} = \sum_i m_i^2 |U_{ei}|^2, \quad (5.1)$$

where the second equality holds if unitarity is assumed. The most recent result on the kinematic search for neutrino mass in tritium decay is from KATRIN [54], which sets an upper limit $m_{\nu_e} < 0.45$ eV at 90% CL.

Direct information on neutrino masses can also be obtained from neutrinoless double beta decay $(A, Z) \rightarrow (A, Z + 2) + e^- + e^-$. This process violates lepton number by two units, hence in order to induce the $0\nu\beta\beta$ decay, neutrinos must be Majorana particles. In particular, if the only effective lepton number violation at low energies is induced by a Majorana mass term for neutrinos, the rate of $0\nu\beta\beta$ decay is proportional to the *effective Majorana mass of ν_e* :

$$m_{ee} = \left| \sum_i m_i U_{ei}^2 \right|. \quad (5.2)$$

Currently the strongest bound on $0\nu\beta\beta$ decay lifetimes are obtained with Germanium ($T_{1/2}^{0\nu} > 1.8 \times 10^{26}$ yr) by GERDA [55] and with Xenon ($T_{1/2}^{0\nu} > 3.8 \times 10^{26}$ yr) by KamLAND-Zen [56]. Depending on the assumed nuclear matrix elements, these correspond to 90% CL limits of $m_{ee} \lesssim 0.079\text{--}0.180$ eV [55] and $m_{ee} \lesssim 0.028\text{--}0.122$ eV [56], respectively.

Finally, neutrino masses also have effects in cosmology. In general, cosmological data mostly gives information on the sum of the neutrino masses, $\sum m_\nu$, while it has very little to say on their mixing structure and on the ordering of the mass states. At present, no positive evidence of the cosmological effect of a non-zero neutrino mass has been observed, which results into upper bounds on $\sum m_\nu$ in the range of $\sum m_\nu \lesssim 0.04\text{--}0.3$ eV (see, *e.g.*, Refs. [57, 58] and references therein for post-DESI [59] global analyses) depending on, *e.g.*, the cosmological data included in the analysis, assumptions on the cosmological model, the statistical approach, the treatment of systematics, or parameter priors.

Within the 3ν -mixing scenario, for each mass ordering, the values of these observables can be directly predicted in terms of the parameters determined in the global oscillation analysis and a single mass scale, which is usually taken to be the lightest neutrino mass m_0 . In addition, the prediction for m_{ee} also depends on the unknown Majorana phases:

$$m_{\nu_e} = \sqrt{m_1^2 c_{13}^2 c_{12}^2 + m_2^2 c_{13}^2 s_{12}^2 + m_3^2 s_{13}^2}, \quad (5.3)$$

$$m_{ee} = \left| m_1 c_{13}^2 c_{12}^2 e^{2i(\alpha_1 - \delta_{\text{CP}})} + m_2 c_{13}^2 s_{12}^2 e^{2i(\alpha_2 - \delta_{\text{CP}})} + m_3 s_{13}^2 \right|, \quad (5.4)$$

$$\sum m_\nu = m_1 + m_2 + m_3, \quad (5.5)$$

$$\text{with } \begin{cases} \text{NO:} & m_1 = m_0, & m_2 = \sqrt{m_0^2 + \Delta m_{21}^2}, & m_3 = \sqrt{m_0^2 + \Delta m_{3\ell}^2}, \\ \text{IO:} & m_3 = m_0 & m_2 = \sqrt{m_0^2 - \Delta m_{3\ell}^2}, & m_1 = \sqrt{m_0^2 - \Delta m_{3\ell}^2 - \Delta m_{21}^2}, \end{cases} \quad (5.6)$$

We show in the upper panels in Fig. 12 the 95% CL allowed ranges for these three probes obtained from the projection of the results of the NuFIT 6.0 global oscillation analysis as a function of m_0 . The larger width of the regions for the m_{ee} predictions is due to the unknown Majorana phases. The regions are shown including only the information from the oscillation data (void regions) and also in combination with the results from KATRIN (filled regions). For the latter, we build a χ^2 function trivially based on their quoted result $m_{\nu_e}^2 = -0.14_{-0.15}^{+0.13}$ eV under the assumptions of Gaussianity, applicability of Wilks' theorem (despite the physical boundary $m_{\nu_e}^2 \geq 0$), and quadratic systematics.²

²Under these assumptions, $\chi^2(m_{\nu_e}) = (m_{\nu_e}^2 + 0.14)^2 / 0.13^2$ yields a 90% CL upper bound $m_{\nu_e} \leq 0.35$ eV which lies in between the bounds $m_{\nu_e} \leq 0.45$ eV and $m_{\nu_e} \leq 0.31$ eV obtained by the collaboration with the Likhov-Tkachov and Feldman-Cousins methods, respectively.

Using the above expressions, one can substitute m_0 by any of the three probes in the expressions of the other two. Thus, within the three-neutrino mixing scenario the predicted values for these three probes are strongly correlated. We show in the lower panels in Fig. 12 the present status of these correlations. As those panels show, with a positive determination of two of these probes one can in principle obtain information on the value of the Majorana phases and/or the mass ordering [60, 61]. Furthermore, a sufficiently strong upper bound can provide information about the ordering of the states [62].

Quantitatively, the global analysis of oscillation data together with the bound from the KATRIN experiment implies that at 95% CL

$$0.00085 \text{ eV} \leq m_{\nu_e} \leq 0.4 \text{ eV} \text{ for NO}, \quad 0.048 \text{ eV} \leq m_{\nu_e} \leq 0.4 \text{ eV} \text{ for IO}, \quad (5.7)$$

$$0.058 \text{ eV} \leq \sum m_\nu \leq 1.2 \text{ eV} \text{ for NO}, \quad 0.098 \text{ eV} \leq \sum m_\nu \leq 1.2 \text{ eV} \text{ for IO} \quad (5.8)$$

and for Majorana neutrinos also

$$0 \leq m_{ee} \leq 0.41 \text{ eV} \text{ for NO}, \quad 0.015 \text{ eV} \leq m_{ee} \leq 0.41 \text{ eV} \text{ for IO}. \quad (5.9)$$

6 Summary

We have presented an updated global analysis of world oscillation data up to September 2024 as listed in Appendix A. Our results are presented in two versions: «IC19 w/o SK-atm» including all the data for which enough information is available to perform an independent accurate fit, and «IC24 with SK-atm» which includes χ^2 data tables provided by the Ice-Cube and Super Kamiokande collaborations that we add to our own χ^2 . The global best-fit values as well as 1σ and 3σ ranges for all parameters are given in Table 1. The main results can be summarized as follows:

- The determination of the parameters θ_{12} , θ_{13} , Δm_{21}^2 , and $|\Delta m_{3\ell}^2|$ is very stable, with Gaussian χ^2 profiles up to high CL. The relative precision at 3σ for these parameters is about 13%, 8%, 16%, (5–6)%, respectively.
- For θ_{23} the precision at 3σ is still about 20%, and the determination suffers from the octant ambiguity. There is a slight preference for the second octant, $\theta_{23} > 45^\circ$, (except for NO and the «IC24 with SK-atm» data) but for all combinations of datasets and mass orderings, the local minimum in the other octant always has $\Delta\chi^2 < 4$.
- The determination of the leptonic CP phase δ_{CP} strongly depends on the mass ordering. For NO the best-fit point is very close to the CP-conserving value of 180° (with $\Delta\chi^2 < 1$), and the χ^2 profile is highly non-Gaussian, with some dependence on the two data variants and on the octant of θ_{23} . For IO, the best fit points for both data variants are close to maximal CP violation $\delta_{\text{CP}} = 270^\circ$ (within 1σ), disfavoring CP conservation at 3.6σ (4σ) for the «IC19 w/o SK-atm» («IC24 with SK-atm») analysis.

- Concerning the mass ordering, we find $\Delta\chi_{\text{IO,NO}}^2 = -0.6(6.1)$ for the «IC19 w/o SK-atm» («IC24 with SK-atm») analysis. The indecisive result for the «IC19 w/o SK-atm» analysis emerges from opposite trends in the long-baseline accelerator appearance data from T2K and NOvA on the one hand, and in the combination of the disappearance channels from accelerator and reactor experiments on the other hand. In the former case, the tension between T2K and NOvA for NO has reached 2σ with the latest NOvA update, whereas they are perfectly consistent for IO. Conversely, the determination of $|\Delta m_{3\ell}^2|$ from ν_μ and ν_e disappearance agrees better for NO than for IO. While a sensitivity analysis suggests that global «IC19 w/o SK-atm» data has a median sensitivity of 2.5σ (2.8σ) to reject NO (IO), the actual result is only 1.7σ (1.4σ) for NO (IO) because of the opposite trends in the data. The addition of IC24 and SK-atm data provides additional preference for NO leading to the above quoted result of $\Delta\chi_{\text{IO,NO}}^2 = 6.1$.

We provide also updated ranges and correlations for the effective parameters sensitive to the absolute neutrino mass from β -decay, neutrinoless double-beta decay, and cosmology. All results and supplementary material such as additional figures and data tables are provided at the NuFit webpage [32].

Acknowledgments

We would like to thank Tetiana Kozynets and Philipp Eller for useful discussions about the IceCube simulation. This project is funded by USA-NSF grant PHY-2210533 and by the European Union’s through the Horizon 2020 research and innovation program (Marie Skłodowska-Curie grant agreement 860881-HIDDeN) and the Horizon Europe research and innovation programme (Marie Skłodowska-Curie Staff Exchange grant agreement 101086085-ASYMMETRY), and by ERDF “A way of making Europe”. It also receives support from grants PID2022-126224NB-C21, PID2022-142545NB-C21, PID2021-123703NB-C21, “Unit of Excellence Maria de Maeztu 2020-2023” award to the ICC-UB CEX2019-000918-M, grant IFT “Centro de Excelencia Severo Ochoa” CEX2020-001007-S funded by MCIN/AEI/10.13039/501100011033, as well as from grants 2021-SGR-249 (Generalitat de Catalunya) and from Basque Government (IT1628-22) grant. IMS is supported by the STFC under Grant No. ST/X003167/1. Part of this work used the Solaris cluster, acquired through the Basque Government IT1628-22 grant.

A List of data used in the analysis

Solar experiments

- ⇒ *External information:* Standard Solar Models [10].
- Chlorine total rate [63], 1 data point.
 - Gallex & GNO total rates [64], 2 data points.

- SAGE total rate [65], 1 data point.
 - SK1 1496-day energy and zenith spectrum [66], 44 data points.
 - SK2 791-day energy and day/night spectrum [45], 33 data points.
 - SK3 548-day energy and day/night spectrum [67], 42 data points.
- ⇒ SK4 2970-day energy and day/night spectrum [11], 46 data points.
- SNO combined analysis [68], 7 data points.
 - Borexino Phase-I 741-day low-energy data [69], 33 data points.
 - Borexino Phase-I 246-day high-energy data [70], 6 data points.
- ⇒ Borexino Phase-II 1292-day low-energy data [12], 192 data points.
- ⇒ Borexino Phase-III 1432-day low-energy data [13], 120 data points.

Atmospheric experiments

- *External information:* Atmospheric neutrino fluxes [71].
- ⇒ IC19 IceCube/DeepCore 3-year data (2012-2015) [19, 20], 140 data points.
- ⇒ IC24 IceCube/DeepCore 9.3-year data (2012-2021) χ^2 map [23, 24] added to our global analysis.
- ⇒ SK1-5 484.2 kiloton-year data [21], χ^2 map [22] added to our global analysis.

Reactor experiments

- ⇒ KamLAND separate DS1, DS2, DS3 spectra [72] with Daya Bay reactor ν fluxes [14], 69 data points.
- ⇒ SNO+ spectrum from partial fill 114 ton-yr [15] data and full fill 286 ton-yr data [16, 17], 17 data points.
- Double-Chooz FD/ND spectral ratio, with 1276-day (FD), 587-day (ND) exposures [73], 26 data points.
- ⇒ Daya Bay 3158-day separate EH1, EH2, EH3 spectra [18], 78 data points.
- Reno 2908-day FD/ND spectral ratio [74], 45 data points.

Accelerator experiments

- MINOS 10.71×10^{20} pot ν_μ -disappearance data [75], 39 data points.
 - MINOS 3.36×10^{20} pot $\bar{\nu}_\mu$ -disappearance data [75], 14 data points.
 - MINOS 10.6×10^{20} pot ν_e -appearance data [76], 5 data points.
 - MINOS 3.3×10^{20} pot $\bar{\nu}_e$ -appearance data [76], 5 data points.
- ⇒ T2K 21.4×10^{20} pot ν_μ -disappearance data [2], 28 data points.
- ⇒ T2K 21.4×10^{20} pot ν_e -appearance data [2], 9 data points for the CCQE and 7 data points for the CC1 π samples.
- ⇒ T2K 16.3×10^{20} pot $\bar{\nu}_\mu$ -disappearance data [77], 19 data points.
- ⇒ T2K 16.3×10^{20} pot $\bar{\nu}_e$ -appearance data [78], 9 data points.
- ⇒ NOvA 26.6×10^{20} pot ν_μ -disappearance data [3], 22 data points.
- ⇒ NOvA 26.6×10^{20} pot ν_e -appearance data [3], 15 data points.
- NOvA 12.5×10^{20} pot $\bar{\nu}_\mu$ -disappearance data [79], 76 data points.
 - NOvA 12.5×10^{20} pot $\bar{\nu}_e$ -appearance data [79], 13 data points.

B IceCube 2019

The IceCube analysis (IC19) is based on Analysis A from Refs. [19, 20]. This analysis uses data collected over 3-years, from April 2012 to May 2015. Following the public data release [80], we computed the expected number of events for each bin, where the reconstructed energy is logarithmically distributed between 5.6 GeV and 56 GeV across eight bins, and the reconstructed cosine of zenith angle is distributed between -1 and $+1$ across ten bins. The events are categorized into two particle identification (PID) types: tracks and cascades. The expected number of events in each bin is given by

$$N_i = T \sum_{\alpha} \sum_{\text{MC}} \phi_{\alpha}^{\text{atm}}(E_{\nu}, \cos \theta) P_{\alpha\beta}(E_{\nu}, \cos \theta) A_{\beta}^{\text{eff}} \quad (\text{B.1})$$

where the sum is performed over all the Monte Carlo simulated events that contribute to the i -th bin and over all initial flavor states, corresponding to electron and muon neutrinos in the case of atmospheric neutrinos. For the atmospheric neutrino flux, we used the Honda flux tables [71] with the energy spectra modified by a factor of $(E_{\nu}/5 \text{ GeV})^{-0.05}$. Both the flux and the oscillation probabilities are evaluated at the true energy and zenith of the simulated events. The constant T denotes the total data-taking time. In addition to the expected event distribution, each bin includes a contribution from the atmospheric muon background, determined by binning the simulated muon background events provided in the public release.

The event distribution in each bin is modified by the detector systematics, which account for the uncertainties in the detector response. These uncertainties include factors such as optical absorption, photon scattering in the ice, DOM efficiency, and the coincidence in reconstruction between neutrinos and atmospheric muons. The systematics are applied to the event distribution as multiplicative reweighting factors for each bin. We have incorporated these uncertainties into our analysis using the information provided in the data release and taking the variable called `reco_coszen` as the negative of the reconstructed zenith angle ($-\cos\theta_{rec}$). These systematics apply to both the event and background distributions. For the uncertainties, we used the values specified in the data release. For the nominal prediction, we assumed that the event distribution is corrected by the offset plus $5 \times \text{opt_eff_lateral}$.

In addition to detector-related systematics, the analysis incorporates uncertainties associated with the atmospheric neutrino flux. These uncertainties are accounted for as follows:

- Normalization: An uncertainty of 100% was assumed, although the results remain consistent when this parameter is left free.
- Initial flavor composition: A 18% uncertainty was included to account for variations in the initial composition of electron and muon neutrinos.
- Neutrino to antineutrino ratio: An uncertainty of 25% was applied to account for variations in the relative flux of neutrinos and antineutrinos.
- Energy dependence of the flux: This uncertainty is parameterized using the factor $(E_\nu/E_0)^\gamma$, with $E_0 = 5$ GeV. The central value of γ is set to zero, and an uncertainty of 5% is applied.
- Upward vs. horizontal flux ratio: A 10% uncertainty was assumed to account for directional asymmetries in the atmospheric neutrino flux.

Assuming a Gaussian χ^2 distribution and noting that the variable `reco_coszen` in the data corresponds to the negative of `reco_coszen` in the simulated events, we have computed IceCube’s sensitivity to Δm_{32}^2 and $\sin^2\theta_{23}$. The results are presented in Fig. 13, alongside a comparison with the findings from Analysis A of [20]. By comparing the best-fit points for the two neutrino mass orderings we obtain a non-significant preference for the normal ordering with a difference of 0.7 units in χ^2 , in excellent agreement with the corresponding result 0.738 reported in ref. [19].

C Assumed true values for the MO test

As mentioned in Sec. 3.3, the values of T_0^o — and therefore the distribution of T — depend on the unknown true value of the oscillation parameters, see Eq. (3.5). In principle, one needs to consider the distribution of T for all possible values of θ^{true} and the final p -value of a MO hypothesis will be given by the largest one among all choices of θ^{true} , *i.e.*, by the

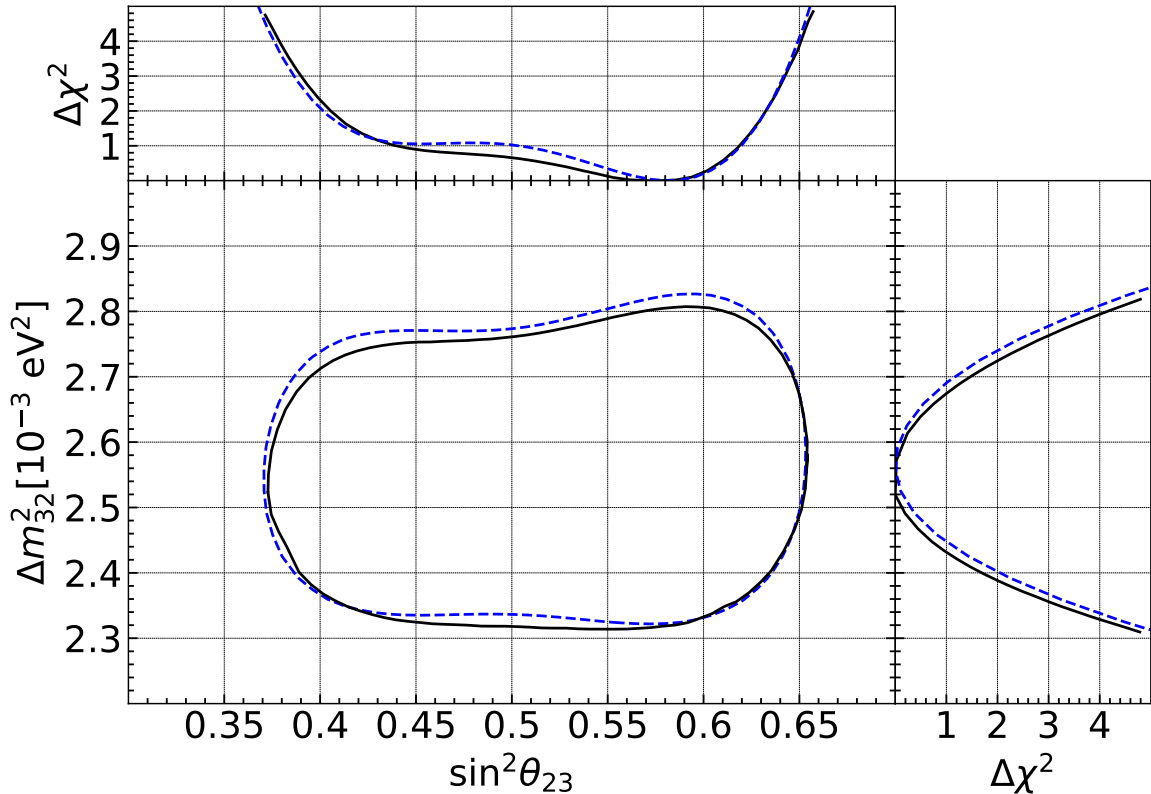


Figure 13. Our fit to IceCube Analysis A (blue dashed lines) is compared to the results from IceCube [20] (black lines).

weakest rejection (see the discussion in Ref. [43]). In the main text, we have assumed that the best fit of the real data is representative of the T -distribution at the unknown true value of θ . Indeed, given the allowed regions of the oscillation parameters, we do not expect T_0 to change significantly if we vary θ^{true} within the allowed regions at reasonable confidence level. The only exception may be the sensitivity of LBL data as a function of δ_{CP} , which is known to affect the MO sensitivity, especially for NO ν A as shown in Fig. 4.

For IO, the global fit constrains δ_{CP} reasonably well, so that we do not expect strong variations of T_0^{IO} for true values of δ_{CP} in its allowed range for IO. However, for NO, a significantly larger range of δ_{CP} is allowed, in particular in correlation with θ_{23} , see Fig. 7. Therefore, the question arises, whether the MO test would give largely different results when considering true values for δ_{CP} and θ_{23} within the allowed region for NO.

From Fig. 4, we see that for $\delta_{\text{CP}} \approx 270^\circ$ and NO, the number of ν_e events in NO ν A is maximal, and its value cannot be obtained by any parameter choice in IO. Therefore, we expect best sensitivity to NO for this value of δ_{CP} . In contrast, values around 0 or 180° can be easily accommodated within IO, and we expect that the sensitivity to NO is weakest around CP-conserving values. We have confirmed this expectation, as we obtain

$$T_0^{\text{NO}}(\delta_{\text{CP}}^{\text{true}} = 270^\circ, \sin^2 \theta_{23}^{\text{true}} = 0.46) = 12.38, \quad (\text{C.1})$$

with all other oscillation parameters kept at their best-fit values. This value is significantly

larger than the value in Eq. (3.6) for the best-fit point with $\delta_{\text{CP}} = 177^\circ$, implying higher sensitivity to reject NO. Actually, for the value in Eq. (C.1) the observed value $T_{\text{obs}} = -0.6$ would imply a p -value for NO of 3.2%. Since values of δ_{CP} around 90° are significantly disfavored also for NO, we do not consider them relevant for the MO test.

To summarize, for relevant choices of the oscillation parameters, the sensitivity to the NO is weakest for values of δ_{CP} around 180° . In turn, for IO, δ_{CP} is sufficiently constrained, and we expect only minor variations of T_0 within the relevant range around 270° . Therefore, it is appropriate to consider the current best fit points to quote the final p -values for both orderings.

References

- [1] T2K, SUPER-KAMIOKANDE collaboration, *First joint oscillation analysis of Super-Kamiokande atmospheric and T2K accelerator neutrino data*, [2405.12488](#).
- [2] T2K collaboration, “T2K experiment status and plans.” Talk given at the *XXXI International Conference on Neutrino Physics and Astrophysics*, Milan, Italy, June 16–22, 2024.
- [3] NOvA collaboration, *New NOvA Results with 10 Years of Data*, .
- [4] I. Esteban, M.C. Gonzalez-Garcia, M. Maltoni, T. Schwetz and A. Zhou, *The fate of hints: updated global analysis of three-flavor neutrino oscillations*, *JHEP* **09** (2020) 178 [[2007.14792](#)].
- [5] P. de Salas, D. Forero, S. Gariazzo, P. Martinez-Mirave, O. Mena, C. Ternes et al., *2020 Global Reassessment of the Neutrino Oscillation Picture*, [2006.11237](#).
- [6] F. Capozzi, E. Lisi, A. Marrone and A. Palazzo, *Current Unknowns in the Three Neutrino Framework*, *Prog. Part. Nucl. Phys.* **102** (2018) 48 [[1804.09678](#)].
- [7] JUNO collaboration, *Potential to Identify the Neutrino Mass Ordering with Reactor Antineutrinos in JUNO*, [2405.18008](#).
- [8] DUNE collaboration, *Long-baseline neutrino oscillation physics potential of the DUNE experiment*, *Eur. Phys. J. C* **80** (2020) 978 [[2006.16043](#)].
- [9] HYPER-KAMIOKANDE collaboration, *Hyper-Kamiokande Design Report*, [1805.04163](#).
- [10] Y. Herrera and A. Serenelli, *Standard Solar Models B23 / SF-III*, 2023. [ZENODO](#), <https://doi.org/10.5281/zenodo.10174170>.
- [11] SUPER-KAMIOKANDE collaboration, *Solar neutrino measurements using the full data period of Super-Kamiokande-IV*, [2312.12907](#).
- [12] BOREXINO collaboration, *First Simultaneous Precision Spectroscopy of pp , ${}^7\text{Be}$, and pep Solar Neutrinos with Borexino Phase-II*, *Phys. Rev. D* **100** (2019) 082004 [[1707.09279](#)].
- [13] BOREXINO collaboration, *Improved Measurement of Solar Neutrinos from the Carbon-Nitrogen-Oxygen Cycle by Borexino and Its Implications for the Standard Solar Model*, *Phys. Rev. Lett.* **129** (2022) 252701 [[2205.15975](#)].
- [14] DAYA BAY collaboration, *Antineutrino energy spectrum unfolding based on the Daya Bay measurement and its applications*, *Chin. Phys. C* **45** (2021) 073001 [[2102.04614](#)].

- [15] SNO+ collaboration, *Initial measurement of reactor antineutrino oscillation at SNO+*, [2405.19700](#).
- [16] SNO+ collaboration, “Reactor Antineutrino Oscillations and Geoneutrinos in SNO+.” Poster 525 at the *XXXI International Conference on Neutrino Physics and Astrophysics*, Milan, Italy, June 16–22, 2024.
- [17] SNO+ collaboration, “Solar Neutrinos: Recent Results and Prospects.” Talk given at the *XXXI International Conference on Neutrino Physics and Astrophysics*, Milan, Italy, June 16–22, 2024.
- [18] DAYA BAY collaboration, *Precision measurement of reactor antineutrino oscillation at kilometer-scale baselines by Daya Bay*, [2211.14988](#).
- [19] ICECUBE collaboration, *Development of an analysis to probe the neutrino mass ordering with atmospheric neutrinos using three years of IceCube DeepCore data*, *Eur. Phys. J. C* **80** (2020) 9 [[1902.07771](#)].
- [20] ICECUBE collaboration, *Measurement of Atmospheric Tau Neutrino Appearance with IceCube DeepCore*, *Phys. Rev. D* **99** (2019) 032007 [[1901.05366](#)].
- [21] SUPER-KAMIOKANDE collaboration, *Atmospheric neutrino oscillation analysis with neutron tagging and an expanded fiducial volume in Super-Kamiokande I-V*, [2311.05105](#).
- [22] SUPERKAMIOKANDE collaboration, *Atmospheric neutrino oscillation analysis with neutron tagging and an expanded fiducial volume in Super-Kamiokande I-V*, 2024. [ZENODO](#), <https://doi.org/0.5281/zenodo.8401262>.
- [23] ICECUBE collaboration, *Measurement of atmospheric neutrino oscillation parameters using convolutional neural networks with 9.3 years of data in IceCube DeepCore*, [2405.02163](#).
- [24] ICECUBE collaboration, *Data release for neutrino oscillation parameters using convolutional neural networks with 9.3 years of data in icecube deepcore*, 2024. .
- [25] I. Esteban, M.C. Gonzalez-Garcia, A. Hernandez-Cabezudo, M. Maltoni and T. Schwetz, *Global analysis of three-flavour neutrino oscillations: synergies and tensions in the determination of θ_{23} , δ_{CP} , and the mass ordering*, *JHEP* **01** (2019) 106 [[1811.05487](#)].
- [26] Z. Maki, M. Nakagawa and S. Sakata, *Remarks on the unified model of elementary particles*, *Prog. Theor. Phys.* **28** (1962) 870.
- [27] M. Kobayashi and T. Maskawa, *CP Violation in the Renormalizable Theory of Weak Interaction*, *Prog. Theor. Phys.* **49** (1973) 652.
- [28] N. Cabibbo, *Time Reversal Violation in Neutrino Oscillation*, *Phys. Lett.* **72B** (1978) 333.
- [29] S.M. Bilenky, J. Hosek and S.T. Petcov, *On Oscillations of Neutrinos with Dirac and Majorana Masses*, *Phys. Lett.* **B94** (1980) 495.
- [30] V.D. Barger, K. Whisnant and R.J.N. Phillips, *CP Violation in Three Neutrino Oscillations*, *Phys. Rev. Lett.* **45** (1980) 2084.
- [31] P. Langacker, S.T. Petcov, G. Steigman and S. Toshev, *On the Mikheev-Smirnov-Wolfenstein (MSW) Mechanism of Amplification of Neutrino Oscillations in Matter*, *Nucl. Phys.* **B282** (1987) 589.
- [32] “NuFit webpage.” <http://www.nu-fit.org>.
- [33] M.C. Gonzalez-Garcia and C. Pena-Garay, *Three neutrino mixing after the first results from K2K and KamLAND*, *Phys. Rev.* **D68** (2003) 093003 [[hep-ph/0306001](#)].

- [34] P.I. Krastev and S.T. Petcov, *Resonance Amplification and t Violation Effects in Three Neutrino Oscillations in the Earth*, *Phys. Lett.* **B205** (1988) 84.
- [35] C. Jarlskog, *Commutator of the Quark Mass Matrices in the Standard Electroweak Model and a Measure of Maximal CP Violation*, *Phys.Rev.Lett.* **55** (1985) 1039.
- [36] PARTICLE DATA GROUP collaboration, *Review of particle physics*, *Phys. Rev. D* **110** (2024) 030001.
- [37] J. Elefant and T. Schwetz, *On the determination of the leptonic CP phase*, *JHEP* **09** (2015) 016 [[1506.07685](#)].
- [38] L. Wolfenstein, *Neutrino oscillations in matter*, *Phys. Rev.* **D17** (1978) 2369.
- [39] M. Maltoni and T. Schwetz, *Testing the Statistical Compatibility of Independent Data Sets*, *Phys. Rev.* **D68** (2003) 033020 [[hep-ph/0304176](#)].
- [40] H. Nunokawa, S.J. Parke and R. Zukanovich Funchal, *Another Possible Way to Determine the Neutrino Mass Hierarchy*, *Phys. Rev.* **D72** (2005) 013009 [[hep-ph/0503283](#)].
- [41] H. Minakata, H. Nunokawa, S.J. Parke and R. Zukanovich Funchal, *Determining Neutrino Mass Hierarchy by Precision Measurements in Electron and Muon Neutrino Disappearance Experiments*, *Phys. Rev.* **D74** (2006) 053008 [[hep-ph/0607284](#)].
- [42] M. Blennow and T. Schwetz, *Determination of the Neutrino Mass Ordering by Combining Pingu and Daya Bay II*, *JHEP* **09** (2013) 089 [[1306.3988](#)].
- [43] M. Blennow, P. Coloma, P. Huber and T. Schwetz, *Quantifying the sensitivity of oscillation experiments to the neutrino mass ordering*, *JHEP* **03** (2014) 028 [[1311.1822](#)].
- [44] X. Qian, A. Tan, W. Wang, J.J. Ling, R.D. McKeown and C. Zhang, *Statistical Evaluation of Experimental Determinations of Neutrino Mass Hierarchy*, *Phys. Rev. D* **86** (2012) 113011 [[1210.3651](#)].
- [45] SUPER-KAMIOKANDE collaboration, *Solar neutrino measurements in Super-Kamiokande-II*, *Phys. Rev.* **D78** (2008) 032002 [[0803.4312](#)].
- [46] N. Grevesse and A.J. Sauval, *Standard Solar Composition*, *Space Sci. Rev.* **85** (1998) 161.
- [47] M. Asplund, N. Grevesse, A.J. Sauval and P. Scott, *The Chemical Composition of the Sun*, *ARA&A* **47** (2009) 481 [[0909.0948](#)].
- [48] A. Serenelli, S. Basu, J.W. Ferguson and M. Asplund, *New Solar Composition: The Problem With Solar Models Revisited*, *Astrophys. J.* **705** (2009) L123 [[0909.2668](#)].
- [49] A.M. Serenelli, W.C. Haxton and C. Pena-Garay, *Solar models with accretion. I. Application to the solar abundance problem*, *Astrophys. J.* **743** (2011) 24 [[1104.1639](#)].
- [50] N. Vinyoles, A.M. Serenelli, F.L. Villante, S. Basu, J. Bergström, M.C. Gonzalez-Garcia et al., *A new Generation of Standard Solar Models*, *Astrophys. J.* **835** (2017) 202 [[1611.09867](#)].
- [51] M. Asplund, A.M. Amarsi and N. Grevesse, *The chemical make-up of the Sun: A 2020 vision*, *arXiv e-prints* (2021) arXiv:2105.01661 [[2105.01661](#)].
- [52] E. Magg et al., *Observational constraints on the origin of the elements - IV. Standard composition of the Sun*, *Astron. Astrophys.* **661** (2023) A140 [[2203.02255](#)].
- [53] M.C. Gonzalez-Garcia, M. Maltoni, J.a.P. Pinheiro and A.M. Serenelli, *Status of direct determination of solar neutrino fluxes after Borexino*, *JHEP* **02** (2024) 064 [[2311.16226](#)].

- [54] KATRIN collaboration, *Direct neutrino-mass measurement based on 259 days of KATRIN data*, [2406.13516](#).
- [55] GERDA collaboration, *Final Results of GERDA on the Search for Neutrinoless Double- β Decay*, *Phys. Rev. Lett.* **125** (2020) 252502 [[2009.06079](#)].
- [56] KAMLAND-ZEN collaboration, *Search for Majorana Neutrinos with the Complete KamLAND-Zen Dataset*, [2406.11438](#).
- [57] J.-Q. Jiang, W. Giarè, S. Gariazzo, M.G. Dainotti, E. Di Valentino, O. Mena et al., *Neutrino cosmology after DESI: tightest mass upper limits, preference for the normal ordering, and tension with terrestrial observations*, [2407.18047](#).
- [58] D. Naredo-Tuero, M. Escudero, E. Fernández-Martínez, X. Marcano and V. Poulin, *Living at the Edge: A Critical Look at the Cosmological Neutrino Mass Bound*, [2407.13831](#).
- [59] DESI collaboration, *DESI 2024 VI: Cosmological Constraints from the Measurements of Baryon Acoustic Oscillations*, [2404.03002](#).
- [60] G.L. Fogli, E. Lisi, A. Marrone, A. Melchiorri, A. Palazzo, P. Serra et al., *Observables sensitive to absolute neutrino masses: Constraints and correlations from world neutrino data*, *Phys. Rev.* **D70** (2004) 113003 [[hep-ph/0408045](#)].
- [61] S. Pascoli, S.T. Petcov and T. Schwetz, *The Absolute Neutrino Mass Scale, Neutrino Mass Spectrum, Majorana Cp-Violation and Neutrinoless Double-Beta Decay*, *Nucl. Phys.* **B734** (2006) 24 [[hep-ph/0505226](#)].
- [62] S. Gariazzo et al., *Neutrino mass and mass ordering: no conclusive evidence for normal ordering*, *JCAP* **10** (2022) 010 [[2205.02195](#)].
- [63] B.T. Cleveland et al., *Measurement of the solar electron neutrino flux with the Homestake chlorine detector*, *Astrophys. J.* **496** (1998) 505.
- [64] F. Kaether, W. Hampel, G. Heusser, J. Kiko and T. Kirsten, *Reanalysis of the GALLEX solar neutrino flux and source experiments*, *Phys. Lett.* **B685** (2010) 47 [[1001.2731](#)].
- [65] SAGE collaboration, *Measurement of the solar neutrino capture rate with gallium metal. III: Results for the 2002–2007 data-taking period*, *Phys. Rev.* **C80** (2009) 015807 [[0901.2200](#)].
- [66] SUPER-KAMIOKANDE collaboration, *Solar neutrino measurements in Super-Kamiokande-I*, *Phys. Rev.* **D73** (2006) 112001 [[hep-ex/0508053](#)].
- [67] SUPER-KAMIOKANDE collaboration, *Solar neutrino results in Super-Kamiokande-III*, *Phys. Rev.* **D83** (2011) 052010 [[1010.0118](#)].
- [68] SNO collaboration, *Combined Analysis of All Three Phases of Solar Neutrino Data from the Sudbury Neutrino Observatory*, *Phys. Rev.* **C88** (2013) 025501 [[1109.0763](#)].
- [69] BOREXINO collaboration, *Precision measurement of the ^7Be solar neutrino interaction rate in Borexino*, *Phys. Rev. Lett.* **107** (2011) 141302 [[1104.1816](#)].
- [70] BOREXINO collaboration, *Measurement of the solar ^8B neutrino rate with a liquid scintillator target and 3 MeV energy threshold in the Borexino detector*, *Phys. Rev.* **D82** (2010) 033006 [[0808.2868](#)].
- [71] M. Honda, M. Sajjad Athar, T. Kajita, K. Kasahara and S. Midorikawa, *Atmospheric Neutrino Flux Calculation Using the Nrlmsise-00 Atmospheric Model*, *Phys. Rev.* **D92** (2015) 023004 [[1502.03916](#)].

- [72] KAMLAND collaboration, *Reactor On-Off Antineutrino Measurement with Kamland*, *Phys. Rev. D* **88** (2013) 033001 [[1303.4667](#)].
- [73] T. Bezerra, “New Results from the Double Chooz Experiment.” Talk given at the *XXIX International Conference on Neutrino Physics and Astrophysics*, Chicago, USA, June 22–July 2, 2020 (online conference) [doi.org/10.5281/zenodo.3959542](#).
- [74] J. Yoo, “RENO.” Talk given at the *XXIX International Conference on Neutrino Physics and Astrophysics*, Chicago, USA, June 22–July 2, 2020 (online conference) [doi.org/10.5281/zenodo.3959698](#).
- [75] MINOS collaboration, *Measurement of Neutrino and Antineutrino Oscillations Using Beam and Atmospheric Data in MINOS*, *Phys. Rev. Lett.* **110** (2013) 251801 [[1304.6335](#)].
- [76] MINOS collaboration, *Electron neutrino and antineutrino appearance in the full MINOS data sample*, *Phys. Rev. Lett.* (2013) [[1301.4581](#)].
- [77] T2K collaboration, *Updated T2K measurements of muon neutrino and antineutrino disappearance using 3.6×10^{21} protons on target*, *Phys. Rev. D* **108** (2023) 072011 [[2305.09916](#)].
- [78] T2K collaboration, *Measurements of neutrino oscillation parameters from the T2K experiment using 3.6×10^{21} protons on target*, *Eur. Phys. J. C* **83** (2023) 782 [[2303.03222](#)].
- [79] A. Himmel, “New Oscillation Results from the NOvA Experiment.” Talk given at the *XXIX International Conference on Neutrino Physics and Astrophysics*, Chicago, USA, June 22–July 2, 2020 (online conference) [doi.org/10.5281/zenodo.3959581](#).
- [80] I. Collaboration, *Icecube 3 year high statistics neutrino oscillation samples*, 2019. [10.21234/AC23-RA43](#).